

1995707801

58-29
17020
p. 40

**THE STUDY OF DOPANT SEGREGATION BEHAVIOR DURING
THE GROWTH OF GaAs IN MICROGRAVITY**

D. H. Matthiesen and J. A. Majewski

Department of Materials Science and Engineering
The Case School of Engineering
Case Western Reserve University, Cleveland, OH 44106

ABSTRACT

An investigation into the segregation behavior of selenium doped gallium arsenide during directional solidification in the microgravity environment was conducted using the Crystal Growth Furnace (CGF) aboard the first United States Microgravity Laboratory (USML-1). The two crystals grown were 1.5 cm in diameter and 16.5 cm in length with an initial melt length of 14 cm. Two translation periods were executed, the first at 2.5 $\mu\text{m/s}$ and after a specified time, which was different between the two experiments, the translation rate was doubled to 5.0 $\mu\text{m/s}$. The translation was then stopped and the remaining sample melt was solidified using a gradient freeze technique in the first sample and a rapid solidification in the second experiment. Measurement of the selenium dopant distribution, using quantitative infra-red transmission imaging, indicates that the first sample initially achieved diffusion controlled growth as desired. However, after about 1 cm of growth, the segregation behavior was driven from a diffusion controlled growth regime to a complete mixing regime. Measurements in the second flight sample indicated that the growth was always in a complete mixing regime. In both experiments, voids in the center line of the crystal, indicative of bubble entrapment, were found to correlate with the position in the crystal when the translation rates were doubled.

INTRODUCTION

Axial Segregation Theory

When an alloy of composition C_0 is solidified, segregation of the solute occurs and is described by the alloy's equilibrium phase diagram [1]. The equilibrium segregation coefficient k_0 , is defined as the ratio of the solute concentration at the interface in the solid to that in the liquid,

thus:
$$k_0 = \frac{C_s^{\text{eq}}}{C_l^{\text{eq}}} \quad (1)$$

If $k_0 < 1$ for an alloy, then solidification causes rejection of solute into the liquid at the solid-liquid interface. There are two limiting theoretical cases: (1) complete convective mixing of the solute in the liquid; and (2) diffusive mixing of the solute in the liquid in the absence of convection.

The solute distribution for the first limiting case of complete mixing in the melt, has been derived by many investigators, most notably by Scheil [2] and Pfann [3]. In their one-dimensional analysis they assume that: (1) there is no diffusion of solute in the solid; (2) the segregation coefficient k_0 , is constant; and (3) there is complete mixing in the liquid. By considering a mass balance of the solute, the composition of the solid as a function of the fraction solidified was derived to be:

$$C_s = k_0 C_0 (1 - f_s)^{(k_0 - 1)} \quad (2)$$

where:

C_s = concentration of the solute in the solid

k_0 = equilibrium segregation coefficient

C_0 = initial concentration in the melt

f_s = fraction solidified

Figure 1 shows the resultant solute distribution in the solid when complete mixing due to convection was present during solidification.

The solute distribution for the second limiting case of diffusion controlled growth, was originally treated by Tiller, Jackson, Rutter and Chalmers [4]. They derived an approximate, time-independent expression to describe the solute concentration in the solid for steady state growth as a function of the distance grown, growth rate, and diffusion coefficient of the solute in the liquid:

$$C_s = C_0 \left[1 - (1 - k_0) \exp\left(-\left(\frac{k_0 R x}{D_l}\right)\right) \right] \quad (3)$$

where:

R = microscopic growth rate

x = distance grown

D_l = diffusion coefficient in the melt

This expression assumes: (a) there is a planar interface; (b) there is no diffusion in the solid; (c) k_0 is a constant; (d) there is no convection in the melt; and (e) that solute is conserved. Also, it is assumed that the rate at which C_s approaches C_0 is a function of growth distance and is proportional to $(C_s - C_0)$.

As Fig. 1 illustrates, growth under these conditions results in a uniform composition profile, except for initial and final transients. The characteristic length for the initial transient D_l/Rk_0 , represents the build up of the solute boundary layer. The characteristic length for the final transient D_l/R , represents the impingement of the solute boundary layer on the end of the crystal.

As can be seen in Fig. 1, a major portion of the crystal grown in a diffusion controlled growth regime would have the desired composition of C_0 . This compares to the complete mixing case, seen in Fig. 1, in which only a small portion of the crystal has the desired composition. Thus, a higher yield of commercially useful crystal would be achieved if diffusion controlled growth could be realized.

Diffusion Controlled Growth

Having established that diffusion controlled growth is desirable from a materials engineering point of view, how can this be achieved? In other words, how can convection in the melt be suppressed or eliminated? A review of this subject is given by Carruthers [5] in which he discusses the factors that influence the stability and types of thermal convective flow patterns and presents the methods employed to control convection. Carruthers examines in detail the importance of thermal boundary conditions and the degree of confinement in determining the nature of thermal convective instabilities. In all types of crystal growth, the factors that influence the type and amount of thermal convection can be characterized by the dimensionless Rayleigh number, NR_a :

$$NR_a = N_{Gr} \times N_{Pr} = \left(\frac{\beta \bar{g} \Delta T L^3}{\alpha \nu} \right) \quad (4)$$

where:

NR_a = Rayleigh number

N_{Gr} = Grashof number

N_{Pr} = Prandtl number

β = thermal expansion coefficient

\bar{g} = effective gravitational constant (g/g_0)

ΔT = change in temperature across L

L = characteristic distance

α = thermal diffusivity

ν = kinematic viscosity

The Rayleigh number is the ratio of buoyancy forces, which lead to the development of convective flow, to the viscous forces, which oppose flow. For small values of the Rayleigh

number, where the viscous forces opposing convection are large, the fluid is stable and thermal convection is absent. At some critical value of the Rayleigh number, the onset of laminar flow occurs and, for increasingly larger Rayleigh numbers, this flow becomes oscillatory and then turbulent in nature. Engineering control of the nature and velocity of these convective flows is achieved by manipulating and controlling the variables described in the Rayleigh number, namely; the characteristic distance; the temperature gradient; and gravity.

The characteristic distance, with a third power dependence, is an obvious starting point as a variable to manipulate in order to eliminate convection in the melt. Kim *et al.* manipulated the melt-to-diameter aspect ratio to control the type and intensity of convection in Te-InSb [6] and Ga-Ge [7] in a top seeded Bridgman system using a gradient freeze growth technique. Holmes and Gatos [8] were able to achieve diffusion controlled growth in small diameter, capillary sized crystals of Ga-Ge in a bottom seeded Bridgman system using a gradient freeze growth technique. As they increased the diameter to larger than 1 mm, the segregation behavior quickly approached the complete mixing regime. Reduction of the characteristic distance then, does not allow for achieving diffusion controlled growth in bulk crystals.

Another variable to manipulate would be the temperature difference across the characteristic distance. In order to solidify single crystals from their melts, it is necessary to remove the heat of solidification from the melt-solid interface during growth. Thus, temperature gradients are required during crystal growth, and the limited manipulation of these temperature differences are typically ineffective in reducing or eliminating convection in the melt. There have however, been several one-dimensional models developed to predict the axial temperature gradients [9], and several two-dimensional models to predict the axial and radial temperature gradients present in the growth system [10]. Although manipulation of temperature gradients has limited effectiveness in eliminating convection in the melt it is an important variable in the generation and multiplication of dislocations and other defects [11].

The final variable in Eq. 4 which can be manipulated to eliminate convective flows in the melt and thus achieve diffusion controlled growth, is the effective gravity term. Experimentation in this area began during the translunar portions of the Apollo 14, 16 and 17 flights [12]. These efforts were continued during the Skylab program with several crystal growth experiments [13].

During the Apollo-Soyuz Test Project (ASTP), Professors Witt and Gatos directed efforts to grow bottom seeded gallium doped germanium using a gradient freeze technique [14]. During growth, current pulses were used to demarcate the melt-solid interface at known time intervals (Peltier Pulsing). These pulses allowed for determination of the interface shape and the growth rate. Single point spreading resistance measurements were used to determine the dopant distribution.

Since there were three growth chambers, none of them were in the thermal center of the furnace, and thus, the melt-solid interface shapes of the crystals were not symmetric. In addition, it was determined that the interface shapes changed throughout growth due to changing thermal loads in the system. Also, it was determined that the growth rate slowly increased during growth and never achieved a steady state value.

The measured dopant distribution quickly increased in value over the first centimeter of growth and then slowly increased throughout the rest of growth. By averaging the measured left periphery, right periphery, and center values, an overall axial distribution was determined. By using the best available material property values from the literature, combined with the measured growth rate data, Witt and Gatos showed that diffusion controlled growth was achieved in the axial direction. In contrast, the ground based experiments showed that the segregation behavior approached that of complete mixing.

The radial dopant distribution data for the crystals grown in space varied by a factor of 3 greater than the radial dopant distribution data for the crystals grown on Earth. This increased radial segregation in the presence of diffusion controlled axial segregation behavior was an unexpected result.

Radial Segregation Theory

The unexpected radial segregation behavior measured in Professors Witt and Gatos's experiment has led to several analytical and numerical investigations into radial segregation behavior. Coriell and Sekerka [15] assumed an interface shape with a radius of curvature expressed as:

$$R = \frac{1}{2} \left(\frac{L^2}{4\Delta d} + \Delta d \right) \quad (5)$$

where:

R = radius of curvature

L = diameter of the crystal

Δd = the interface deflection

With this assumed interface shape, they were able to solve analytically for the radial segregation due to a slightly curved interface, a small Peclet number and a flat interface shape at the ampoule wall. When data from the Witt and Gatos experiment were used, their solution predicted approximately 10 percent radial segregation, which is in qualitative agreement with the measured 300 percent radial segregation data.

Coriell, Sekerka and coworkers [16] followed this paper with a paper in which they combined analytical and numerical results to predict the radial segregation behavior due to large interface deflections, a large Peclet number and a flat interface shape at the ampoule wall.

As part of this program Korpela, Chait and Matthiesen [17] developed an analytic expression for the radial segregation due to small interface deflections, large Peclet numbers and an arbitrary interface shape at the ampoule wall.

Computer Modeling

Numerical investigations were then initiated to provide further insight into the radial segregation behavior. The numerical simulations of Kim, Adornato and Brown [18] have recently shed some insight into the problem of axial and radial segregation behavior with respect to the convection present in the melt. They predict that, initially in a bottom seeded Bridgman-Stockbarger growth system, a two cell torroidal flow pattern will exist, with an intense flow cell near the melt-solid interface. As the flow velocities are decreased, either by microgravity or applied magnetic fields, or both, the two flow cells gradually merge into one large cell. As the flow velocities are further decreased, this one flow cell eventually disappears and diffusion controlled growth is achieved.

An important conclusion of their analysis is that when the two cell patterns become one cell, the axial dopant distribution approaches that of diffusion controlled growth, but the radial segregation increases. It is only after the flow velocities are further reduced that the radial segregation finally decreases, as shown in Fig. 2. When the convective flows are finally suppressed, the radial segregation is controlled by the interface shape, as predicted by Coriell and Sekerka.

I. GROWTH OF Se DOPED GaAs IN MICROGRAVITY

A. Motivation and Goals

Although the work of Professor Brown and his co-workers has provided useful insight to the segregation behavior during the growth of electronic materials, there has been little experimental verification. In fact, the Witt and Gatos experiment is the only experiment which has had all the appropriate data necessary for comparison to these numerical simulations.

The question then arises, can these simulations be used to predict the growth of other materials in microgravity? In 1978 the Committee on Scientific and Technological Aspects of Materials Processing in Space (STAMPS) of the National Research Council [19] issued a report which reviewed the materials processing in space programs done to that date. Among their many conclusions was that, although the growth of germanium on ASTP provided a firm foundation for

the growth of electronic materials in space, it was not possible *a priori* to extrapolate these results to the more technologically interesting III-V and II-VI materials. In addition, the necessary material property values needed to perform applicable numerical simulations that would predict the outcome of processing these materials in space have not been precisely determined, and in some cases, not determined at all.

B. Scientific Objectives

The scientific objectives of these experiments were to determine the following under microgravity conditions:

1) to investigate techniques for obtaining complete axial and radial dopant uniformity during the crystal growth of selenium doped gallium arsenide

2) to use a large melt length-to-melt diameter aspect ratio (9.3:1) initially to investigate steady state segregation behavior and

3) to use a small melt length-to-melt diameter after the above to study the transient segregation behavior during the gradient freeze growth

The third scientific objective would provide a baseline to other experiments which have been conducted in microgravity with this material system.

II. EXPERIMENTAL PROCEDURE

A. Crystal Growth of Sample Charges

The Liquid Encapsulated Czochralski (LEC) grown crystals were oriented $\langle 111 \rangle$ and doped to achieve an average dopant concentration in the grown crystal of $\approx 10^{17}/\text{cm}^3$. These charges were prepared from the *in situ* synthesis and growth of ≈ 800 gm charges of selenium doped gallium arsenide. A layer of boric oxide was used as an encapsulant and a pyrolytic boron nitride (PBN) crucible was used for the growth. An argon overpressure was maintained in the Malvern High Pressure crystal growth system. Typically the seed rotation rate was 10 rpm and the crucible rotation was 0 rpm. The pulling rates were typically 1 $\mu\text{m/s}$.

The single crystal LEC boules were then annealed in flowing argon at 600°C for a 3 hour period and then slowly cooled to room temperature. The boules were then machined to the desired diameter using a diamond coring drill. Typically three cored samples could be obtained from a two inch diameter boule. After coring the samples were cut to length, typically 5-7 cm long, and again annealed to relieve any stresses from the machining process. These crystals were sized to the PBN sleeve by etching with 1:1:1 sulfuric:peroxide:acetic acid to the final diameter.

For the science samples and the first flight and ground truth samples, a total charge would consist of three single crystal doped samples totaling 16.5 cm in length. For the second flight and ground truth samples, which were actually part of the ampoule qualification test program, the charge consisted of a doped single crystal seed and two undoped polycrystalline sections.

B. Ampoule Design and Fabrication

As shown in Fig. 3, each charge consisted of three Liquid Encapsulated Czochralski (LEC) grown crystals. These 1.5 cm in diameter crystals were contained within a pyrolytic boron nitride crucible (sleeve). This sleeve had a 0.035 inch wall and was 18 cm long. The cold end contained a graphite pedestal for positioning the seed crystal. The hot end contained a graphite plunger, which in turn contained a PBN leaf spring assembly. This spring allowed the plunger to advance and retreat as the crystal contracted upon melting and expanded upon freezing. The crystal, graphite and PBN were hermetically sealed into a fused quartz envelope, which minimized the arsenic losses from the GaAs crystal. The ampoule was heated to 250°C under 10 millitorr vacuum before it was finally sealed.

The ampoule was then positioned into a cartridge. This cartridge was made of WC-103 and had an Fe silicide coating on the outside to inhibit thermal oxidation. As shown in Fig. 3, there were six open bead, type-S thermocouples located between the ampoule and the cartridge. The ampoule was positioned to the correct seeding position using zirconia insulation pedestals.

Since the ampoule was determined to contain 2.2 atm of arsenic pressure at the processing temperature of 1260°C [20], the cartridge was filled with argon gas and hermetically sealed to balance this internal ampoule pressure. Thus, even though the fused quartz of the ampoule was in viscous flow at the processing temperature no deformation of the ampoule was expected since the pressure forces on the ampoule balanced one another.

Before delivery each sample ampoule-cartridge assembly (SACA) was X-rayed to determine the exact location of the thermocouples relative to the seed end of the crystal.

C. Experimental Timelines

The experimental timeline for the first experiment is shown in Fig. 4. The experiment consisted of establishing a desired thermal gradient of 15°C/cm across the 2 cm gradient zone of the CGF, with the melt/solid interface located in the center of the gradient zone. The initial location of the crystal in relation to the gradient zone is shown in Fig. 3. Ideally at the fully inserted position, thermocouple T2 would read 1238°C and the seeding melt-solid interface position would be in the center of the gradient zone. This would result in a 14 cm melt length. After a thermal soak, two translation periods were executed, the first at 2.5 $\mu\text{m/s}$ for 4.05 cm and the second at

5.0 $\mu\text{m/s}$ for 4.05 cm. The translation was then stopped and the remaining 5.9 cm sample melt was solidified using a gradient freeze technique, which in a 4 hour period would have an average growth rate of 5.0 $\mu\text{m/s}$.

The experimental timeline for the second experiment is shown in Fig. 5. The experiment consisted of establishing a desired thermal gradient of 15°C/cm across the 2 cm gradient zone of the CGF, with the melt/solid interface located in the center of the gradient zone. The initial location of the crystal in relation to the gradient zone is shown in Fig. 3. Ideally at the fully inserted position, thermocouple T2 would read 1238°C and the seeding melt-solid interface position would be in the center of the gradient zone. This would result in a 14 cm melt length. After a thermal soak, two translation periods were executed, the first at 2.5 $\mu\text{m/s}$ for 3.15 cm and the second at 5.0 $\mu\text{m/s}$ for 3.15 cm. The translation was then stopped and the remaining 7.7 cm sample melt was solidified using a rapid quench by issuing a power off command to the heaters.

In an attempt to measure the growth interface shape and microscopic growth rate, a mechanical pulse was initiated by a solenoid attached to the top of the cartridge at specified times. These times were selected to occur during the steady state growth periods and are indicated in Figs. 4 and 5.

D. Sample Analysis Preparation

After flight each SACA was X-rayed after which the ampoule was removed from the cartridge and inspected. The ampoules were then opened and the GaAs crystals removed. After inspection the GaAs crystals were oriented such that an axial cut made down the axial center of the crystal was parallel to the (211) plane. A 0.070 inch thick (1.778 cm) axial slice was then cut from the crystal and polished both sides to yield a 0.050 inch (1.27 cm) sample. The smaller of the two half cylinders or 'D' sections was cut perpendicular to the axial direction. This yielded approximately 150 0.050 inch (1.27 cm) thick 'D' shaped samples, which are being used for Hall effect measurements. The remaining large half cylinders or 'D' section were lapped with 1 μm alumina.

III. RESULTS AND DISCUSSION

A. As Grown Surface Characterization

All crystals grown in space and on Earth could readily be removed from the PBN sleeve. The surface of the seed could readily be differentiated from the remelt region because the seed had a bright specular finish from the etch used in charge preparation while the remelt region had a dull, matte finish indicative of contact with the PBN sleeve. No free surfaces were observed and the

diameter of the remelt region was constant, thus it is concluded that the PBN spring-graphite plunger did in fact work.

B. Axial Slice Characterization: Lapped Surface

The lapped surface from the first space flight and ground truth experiments are shown in Fig. 6. Here it can be seen that polycrystalline breakdown occurs in both samples during the first translation period. In addition, several large voids appear in the centerline of the flight sample. The first occurrence of these voids corresponds to the translation rate change.

The lapped surfaces from the second space flight and ground truth experiments are shown in Fig. 7. Here too it can be seen that a central void appears in the flight sample. The position of the first occurrence of this void again corresponds to the translation rate change. In addition, during the rapid quench period, voids can be seen in both samples. However, in the flight samples there are only a few large voids while in the ground truth sample there is a distribution of small voids.

The segmented nature of these voids is suggestive of bubbles and it is expected that they were arsenic bubbles at their formation. One explanation of why the bubbles are in the central axis of the flight crystal is that they were formed there, i.e. as the melt-solid interface moved along, arsenic gas came out of solution at the 'cold' interface. In the ground test, the arsenic gas would rise to the top (all ground samples were run in a vertically stabilizing configuration) but in flight the arsenic gas would not and was therefore captured at the growth interface. Following this logic, if the ground tests were run at very large growth rate, then the arsenic bubbles could be trapped at the interface also. There is evidence of this in the rapid quench section of the second ground based sample, shown in Fig. 7.

C. Axial Slice Characterization: Infra-red Transmission

The axial slices were polished on both sides and imaged using a macroscopic infra-red transmission imaging system [21]. Figures 8-11 are montages of the infra-red transmission through the ground truth 1, space flight 1, ground truth 2 and space flight 2 samples.

The meltback position in each sample is clearly seen in the left hand side of each sample. A small portion of each sample is lost due to the presence of the sample holder. The meltback positions for the four samples are compared in Fig. 12. Although the meltback positions of the four samples varied from 3.2 cm to 2.0 cm (i.e. remaining seed material) an analysis of the relative position differences of the seeding thermocouples to that of the thermocouple temperature readings indicates that these differences are strictly due to the relative position differences of the thermocouple and are not due to being processed on the ground or in space.

None of the samples show any evidence of demarcation lines, with the exception of two lines in the first flight sample, Fig. 9. In Fig. 13 the relative position of the seeding interface (s), thermocouples (TCx), translation periods (Tx) and the mechanical pulses (Pxy) are shown. Although a comparison of Fig. 13 with Fig. 9 shows that the relative position of the two demarcation lines are close to P22 and P23, measurement of the growth rate, assuming the time difference between the two pulses, yields a growth rate of $7.5 \mu\text{m/s}$ not $5.0 \mu\text{m/s}$, which was the translation rate during that period. Since these two demarcation line are at the beginning of a void, it is believed instead that they are artifacts from the entrapment of the bubble into the growing crystal.

D. Seeding Interface Shape Measurements

The seeding interfaces are clearly seen in the left hand portion in each sample shown in Figs. 8-11. All seeding interfaces are curved into the liquid. Using an infra-red microscope, a photomicrograph montage of the seeding interface can be constructed, as shown in Fig. 14 for the second space flight and ground truth samples. The seeding interface shape can then be measured.

The four seeding interface shapes are shown in Fig. 15. All the interfaces deflections are approximately the same and are symmetric about the growth axis. This is to be expected since the seeding interface shape is the result of the steady state heat transfer and for a lower Prandtl number fluid the fluid flow does not contribute much to the overall heat transfer. Thus, it is expected that the interface shape and growth rate from the space experiments will be similar to the ground truth experiments.

E. Dopant Distribution Measurements

In Figs. 8-11 variations in the photographic contrast can be seen. Since this is a photograph of an infra-red transmission image, these contrast differences are due to differences in transmission of light through the sample. Since these samples were doped at $1 \times 10^{17}/\text{cm}^3$ with selenium, which is several orders of magnitude larger than any unintentional impurity, it is assumed that these variations in transmission are due to variations in selenium distribution in the samples.

A macro-imaging system based on these assumptions has been developed and a detailed description can be found in the literature [21]. In essence, this system used a CCD camera at a known wavelength on infra-red light ($1.05 \mu\text{m}$) to measure the transmission of the sample. By measuring calibration samples of known transmission with the system, then a transformation can be made from gray level output from the camera to transmission. The transmission can be converted to absorption coefficient by knowing the wavelength (and thus the index of refraction) and the sample thickness. The absorption coefficient can then be converted to free carrier concentration and at room temperature it is assumed that all the free carriers are due to the selenium.

The resultant image of the selenium distribution is approximately 100 pixels wide by 400 pixels long. This corresponds to an area approximately 0.015 cm wide by 0.02 cm long. To determine the average axial dopant distribution the 100 values are averaged across the sample. The overall average free carrier concentration for ground truth 1 and space flight 1 are shown in Figs. 16 and 17. The area of interest in each of these figures is only the first translation period, since the presence of the voids invalidates this measurement technique. Also shown in Figs. 16 and 17 are selected radial distribution plots.

F. Axial Segregation Analysis

In Fig. 18, the average selenium distribution for the first ground based sample is compared to the predicted distribution made using the complete mixing equation (Eqn. 2). As can be seen there is fair agreement in these data.

In Fig. 19, the average selenium distribution for the first flight sample is compared to the predicted distribution made using the diffusion controlled growth equation (Eqn 3). Also plotted is the distribution predicted from the complete mixing equation. As can be seen, the growth starts out following the diffusion controlled growth prediction within the error associated with the precision that the thermal physical property values are known. However, after approximately 0.5 cms the distribution is slowly driven into the complete mixing regime.

G. Radial Segregation Analysis

The radial dopant distributions shown in Figs. 18 and 19 show that for the ground base sample the radial segregation is about 30% - 50%, which would be expected in a sample of this size. In Fig. 19 however, the radial distribution starts out slightly above 20%. This is in excellent agreement with Coriell and Sekerka's second paper (C&S II) as shown in Fig. 20. However, as the growth continues beyond 1 cm, where the axial segregation indicates that the axial distribution is moving to a complete mixing regime, the radial segregation increases to the 30% - 50% range typical of the ground based sample. Thus, the radial segregation completely supports the conclusions derived from the axial segregation data.

I. Comparison to Acceleration Data

Three acceleration measurement experiments were flown as part of this mission: OARE, SAMS and PAS. All of them are experiments in their own right, were conducted for their own reasons and the final data from these experiments has not been released. However, the Principal Investigators [22-24] from these experiments have shared some preliminary data. Of particular interest is, of course, the time period after the start of growth for the first flight experiment.

The data from OARE with an approximate growth scale is shown in Fig. 21. As can be seen there is a large gap in the data in the region of interest. This is because the OARE data analysis

program filters out any large data excursions. This conclusion is confirmed with the data from SAMS shown in Fig. 22 where a large acceleration event occurred at the one hour (≈ 1 cm) point of the experiment.

Although it is left to identify what this particular acceleration event was, it is sufficient to conclude that one did occur. This acceleration event was sufficiently large in amplitude and duration that it drove the segregation behavior of the sample from diffusion controlled growth to that of complete mixing.

CONCLUSIONS

Measurement of the selenium dopant distribution, using quantitative infra-red transmission imaging, indicates that the first sample initially achieved diffusion controlled growth as desired. However, after about 1 cm of growth, the segregation behavior was driven from a diffusion controlled growth regime to a complete mixing regime. Measurements in the second flight sample indicated that the growth was always in a complete mixing regime. In both experiments, voids in the center line of the crystal, indicative of bubble entrapment, were found to correlate with the position in the crystal when the translation rates were doubled.

ACKNOWLEDGMENTS

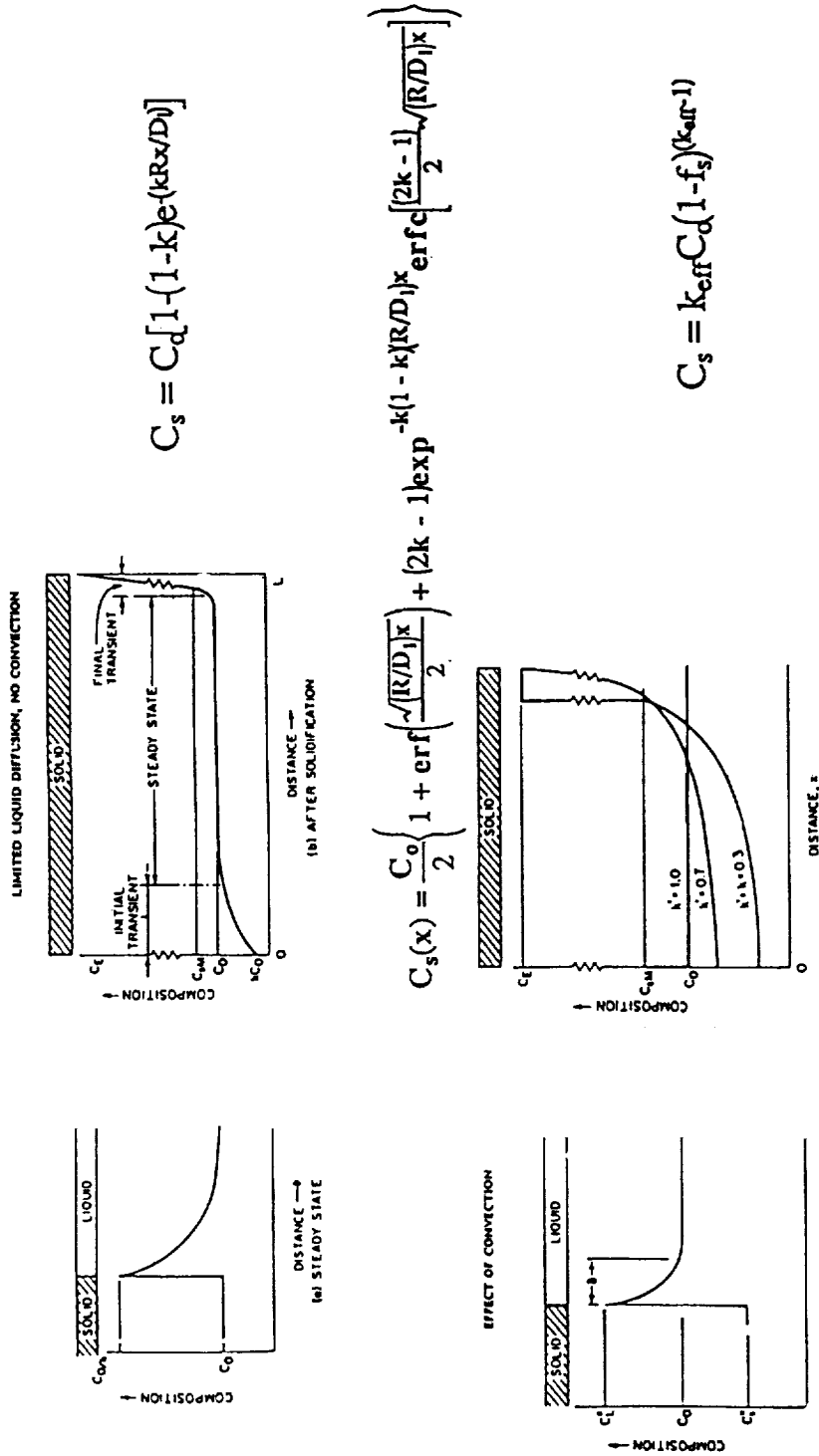
The authors would like to thank the National Aeronautics and Space Administration for their cooperation and enthusiastic support during all stages of these experiments. The following individuals are especially noted for their unwavering efforts in achieving the success of these experiments: Mr. David Schaefer, Project Manager and Dr. Frank Szofran, Project Scientist from the Marshall Space Flight Center and Mr. Joel Kearns, Program Manager from the Microgravity Science and Applications Division of NASA Headquarters. This work was sponsored under NASA-MSFC contract NAS8-39695.

REFERENCES

1. M.C. Flemings, *Solidification Processing*, McGraw-Hill, Inc (1974).
2. E. Schiel, *Z. Metallk.*, 34 (1942) 70.
3. W.G. Pfann, *J. Metals*, 4 (1952) 763.
4. W.A. Tiller, K.A. Jackson, J.W. Rutter and B. Chalmers, *Acta. Met.*, 1 (1953) 428.
5. J.R. Carruthers, in *Preparation and Properties of Solid State Materials*, vol. 3, (1973) 1.

6. K.M. Kim, A.F. Witt and H.C. Gatos, *J. Electrochem. Soc.*, 119 (1972) 1218.
7. K.M. Kim, A.F. Witt, M. Lichtensteiger and H.C. Gatos, *J. Electrochem. Soc.*, 125 (1978) 475.
8. D.E. Holmes and H.C. Gatos, *J. Electrochem. Soc.*, 128 (1981) 429.
9. see for instance
 C.E. Chang and W.R. Wilcox, *J. Crystal Growth*, 21 (1974) 135.
 R.J. Naumann, *J. Crystal Growth*, 58 (1982) 554.
 T. Jasinski, W.M. Rosenow and A.F. Witt, *J. Crystal Growth*, 61 (1983) 710.
10. see for instance
 T.F. Fu and W.R. Wilcox, *J. Crystal Growth*, 48 (1980) 416.
 R.J. Naumann, *J. Crystal Growth*, 58 (1982) 569.
 T. Jasinski, W.M. Rosenow and A.F. Witt, *J. Crystal Growth*, 67 (1984) 173.
 T. Jasinski, W.M. Rosenow and A.F. Witt, *J. Crystal Growth*, 71 (1985) 295.
11. see for instance
 S. Motakef, *J. Crystal Growth*, 98 (1989) 711.
 A.S. Jordan, *J. Crystal Growth*, 49 (1980) 631.
12. R.J. Naumann and H.W. Herring, *Materials Processing in Space: Early Experiments*, NASA SP-443, Washington, DC (1980).
13. Proceedings Third Space Processing Symposium, *Skylab Results: Volume 1*, NASA-Marshall Space Flight Center, M-74-5, June (1974).
14. A.F. Witt, H.C. Gatos, M. Lichtensteiger and C.J. Herman, *J. Electrochem. Soc.*, 125 (1978) 1832.
15. S.R. Coriell and R.F. Sekerka, *J. Crystal Growth*, 46 (1979) 479.
16. S.R. Coriell, R.F. Boisvert, R.G. Rehm and R.F. Sekerka, *J. Crystal Growth*, 54 (1981) 167.
17. S.A. Korpela, A. Chait and D.H. Matthiesen, *J. Crystal Growth*, accepted for publication (1993).
18. D.H. Kim, P.M. Adornato and R.A. Brown, *J. Crystal Growth*, 89 (1988) 339.
19. Committee on Scientific and Technological Aspects of Materials Processing in Space, *Materials Processing In Space*, National Academy of Sciences, Washington DC, (1978).
20. D.H. Matthiesen, *J. Crystal Growth*, accepted for publication (1994).
21. J.A. Majewski and D.H. Matthiesen, *J. Crystal Growth*, accepted for publication (1994).
22. R. Blanchard, OARE Principal Investigator, private communication.
23. R. Delombard, SAMS Principal Investigator, private communication.
24. I. Alexander, PAS Principal Investigator, private communication.

Axial Segregation



The effect of convection in the melt is to increase the segregation in the solid

Figure 1 Solute redistribution during solidification with limited liquid diffusion and no convection. Composition profile during steady-state solidification and composition profile after solidification, top. Solute redistribution during solidification with limited liquid diffusion and convection in the melt. Composition profile during steady-state solidification showing d , the mass boundary layer and composition profile after solidification, bottom. (After Flemings [1]).

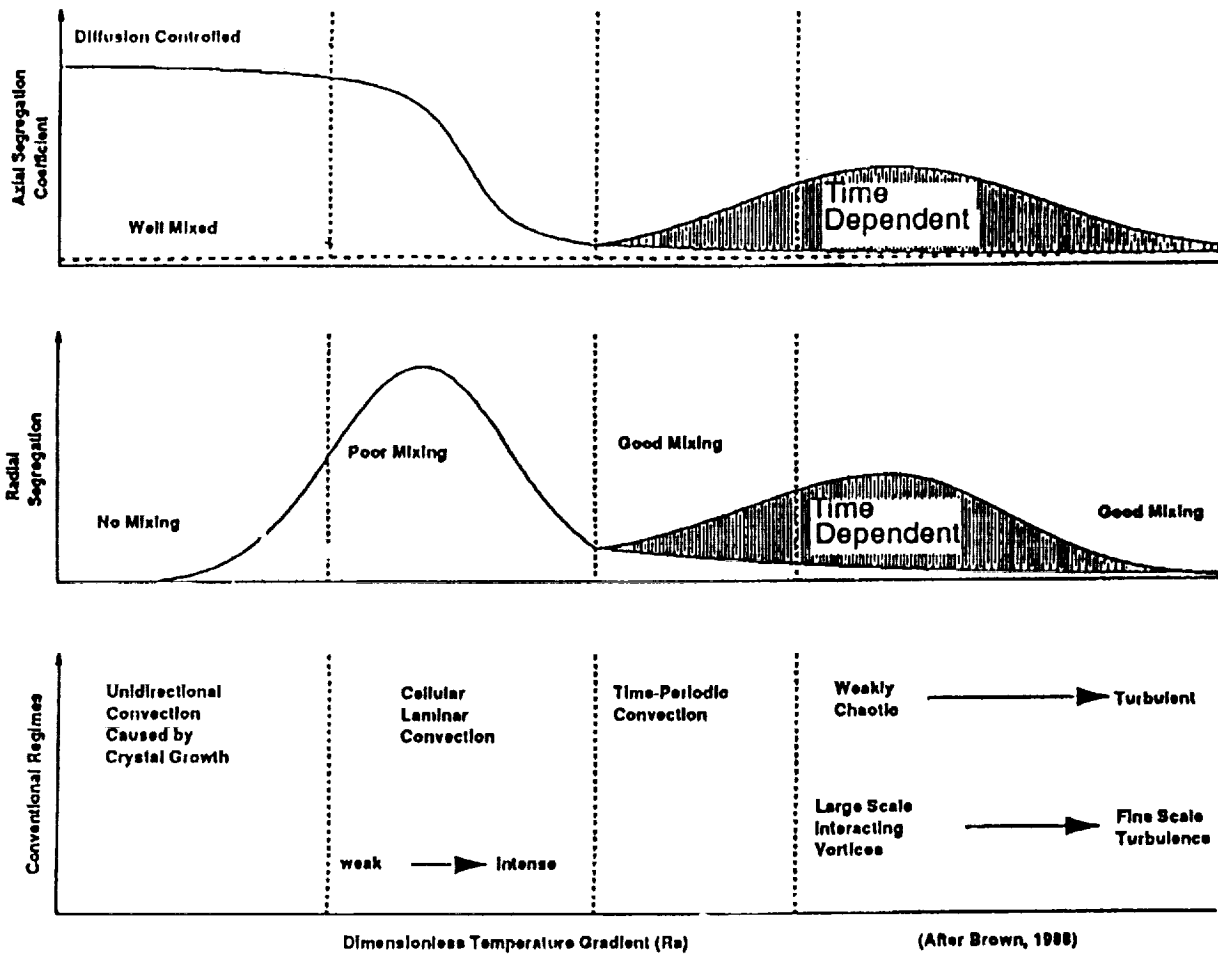


Figure 2 The effect of convection on the axial and radial segregation in a dilute binary system (after Brown [18]).

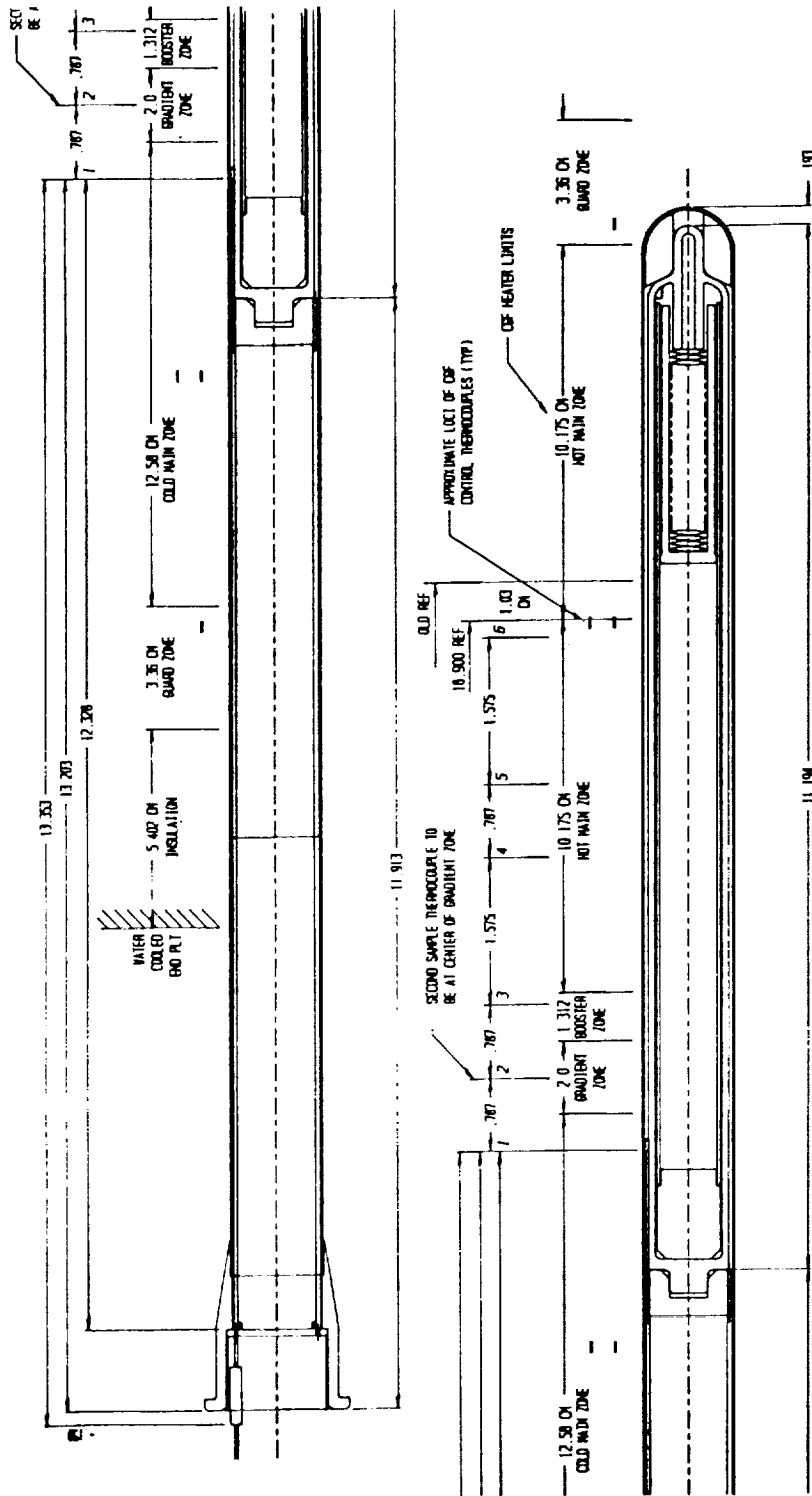


Figure 3 Cross-sectional drawing of the ampoule within the cartridge, together these form the Sample Ampoule Cartridge Assembly (SACA), at the initial seeding position. Also shown are the relative relationship of the sample thermocouples and furnace zone positions.

GTE-GaAs Experiment
Version 5.0
12/18/91

HG=1260°C
HM=1255°C
HB=1255°C
CM=1225°C
CG=1230°C

HG=1235°C
HM=1230°C
HB=1225°C
CM=1225°C
CG=1225°C

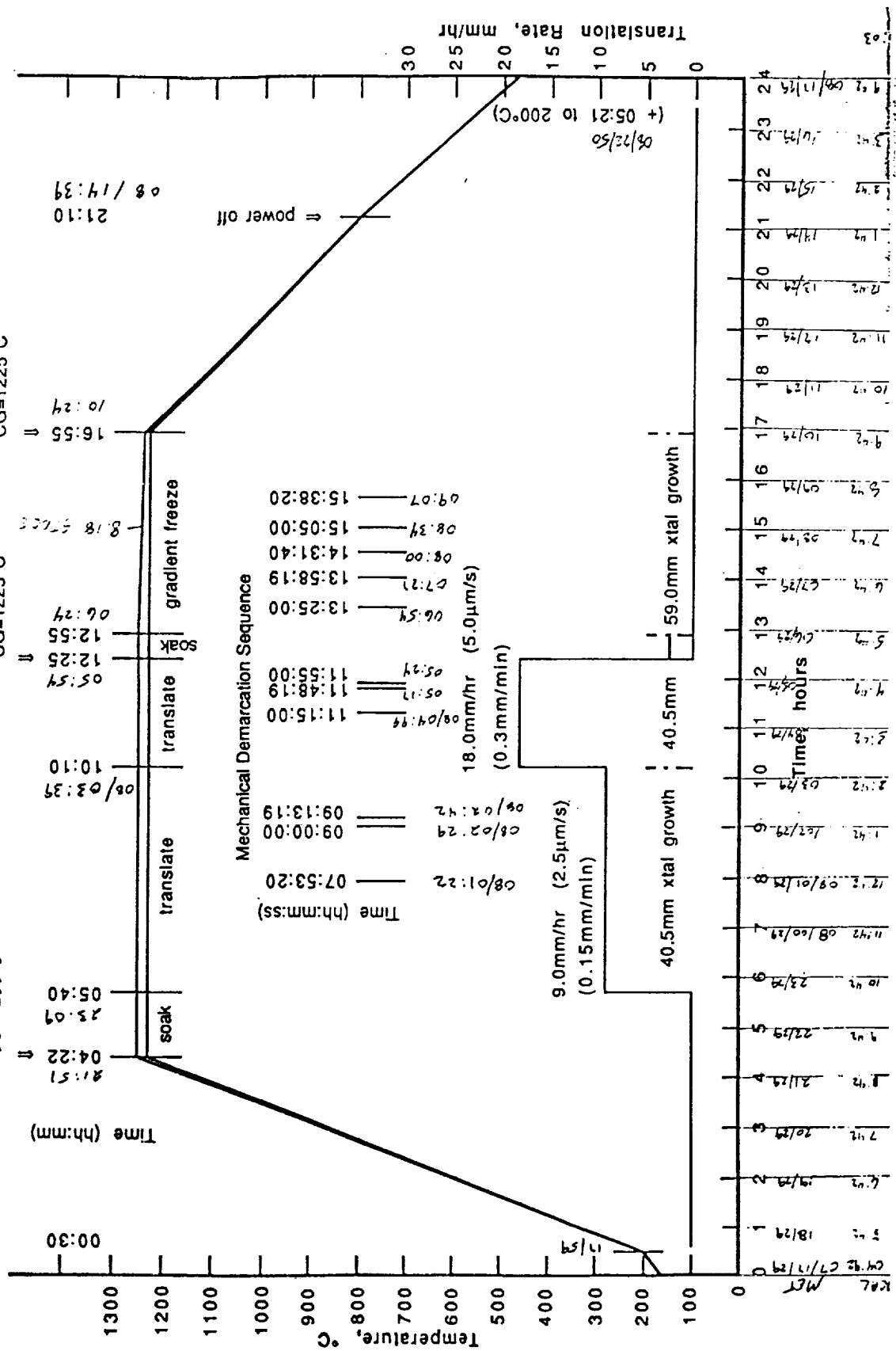


Figure 4 Experimental timeline for the first flight and ground truth experiments. MET times are listed for the flight experiment.

**CWRU-GaAs
Experiment**
Version 6.2
07/04/92

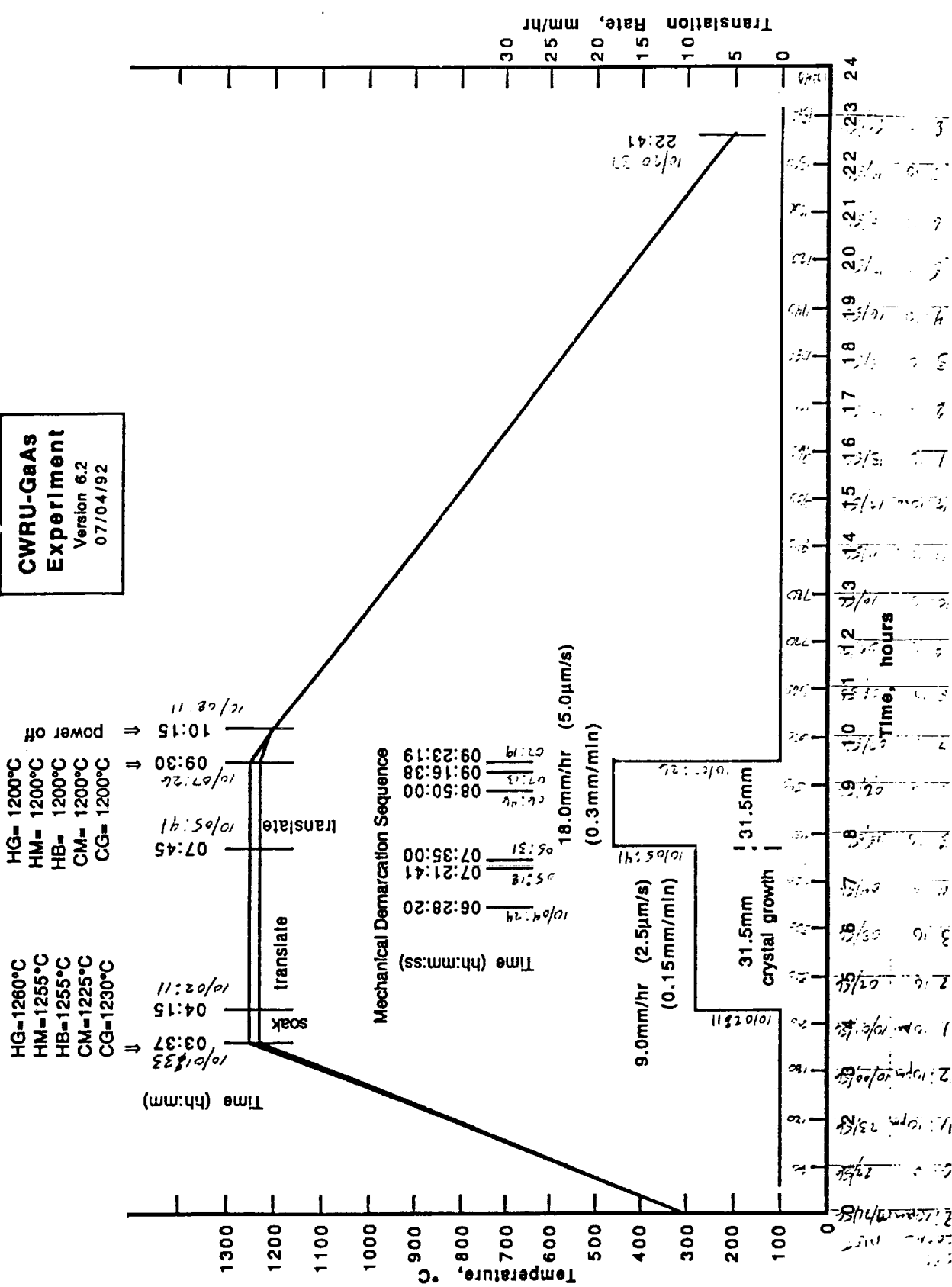


Figure 5 Experimental timeline for the second flight and ground truth experiments. MET times are listed for the flight experiment.

ORIGINAL PAGE IS
OF POOR QUALITY

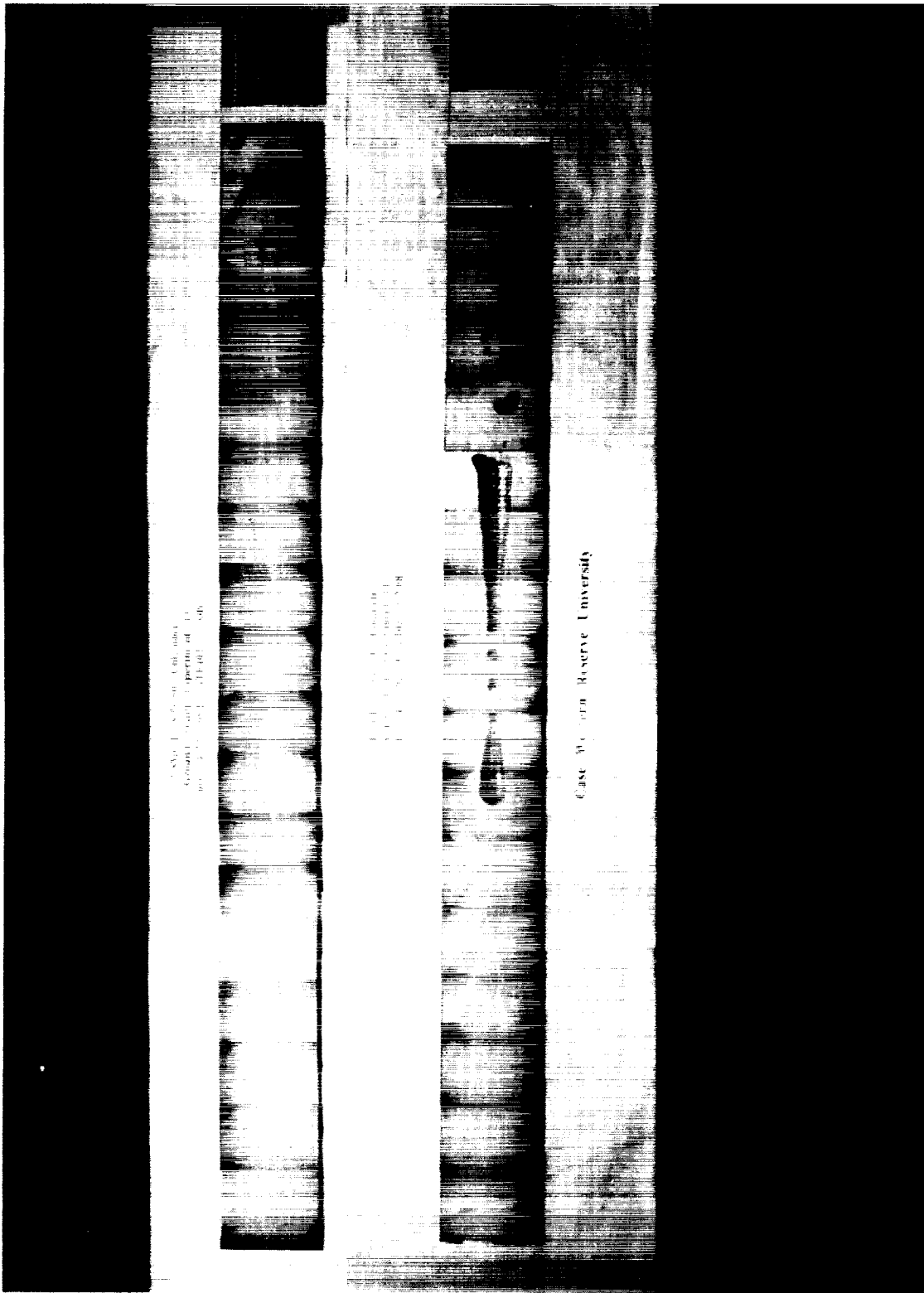


Figure 6 Lapped surface samples from the first flight and ground truth samples.

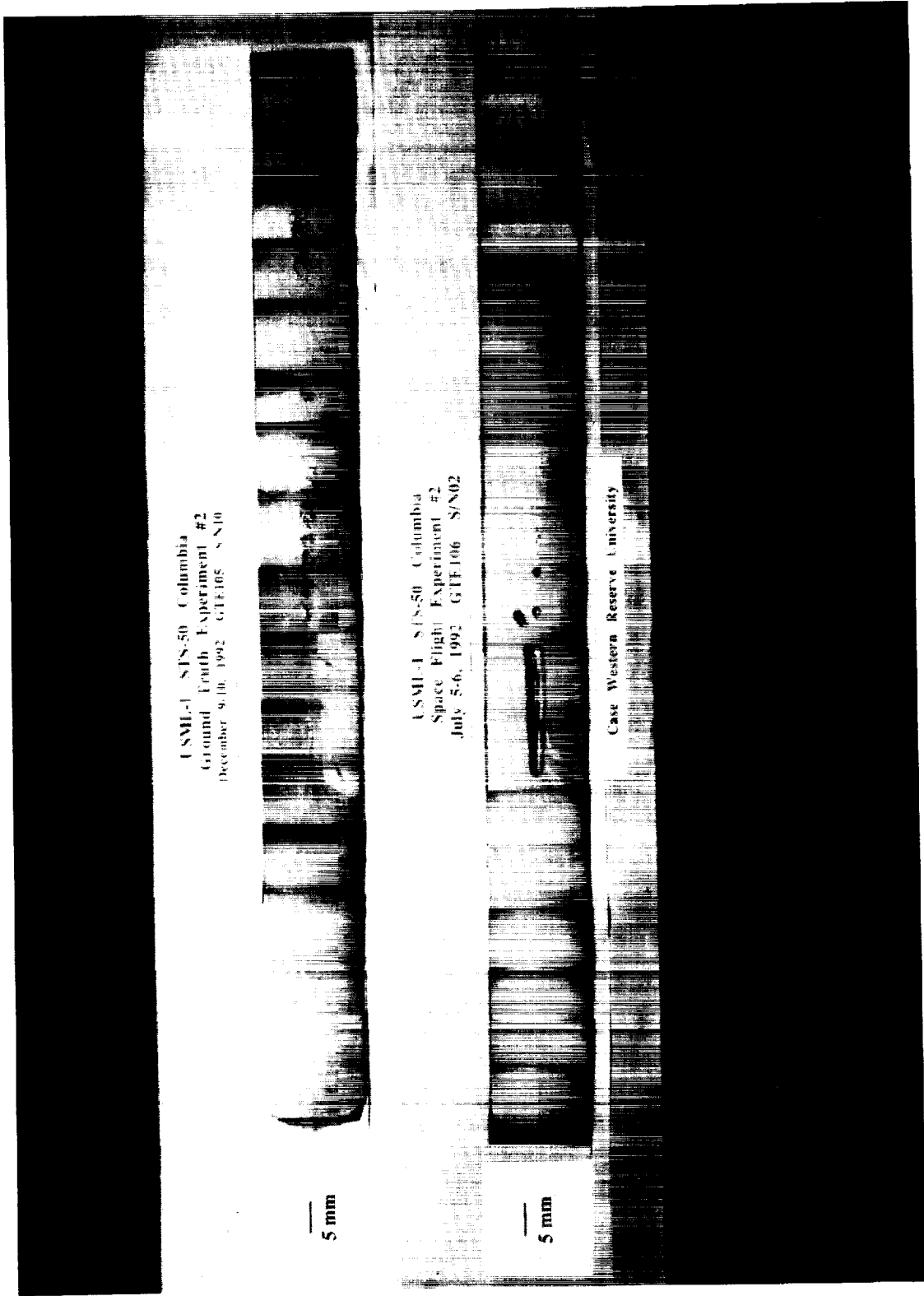


Figure 7 Lapped surface samples from the second flight and ground truth samples.

USMC 81550 Columbia
Experiment #1
COLUMBIA
USMC

Naval Reserve University

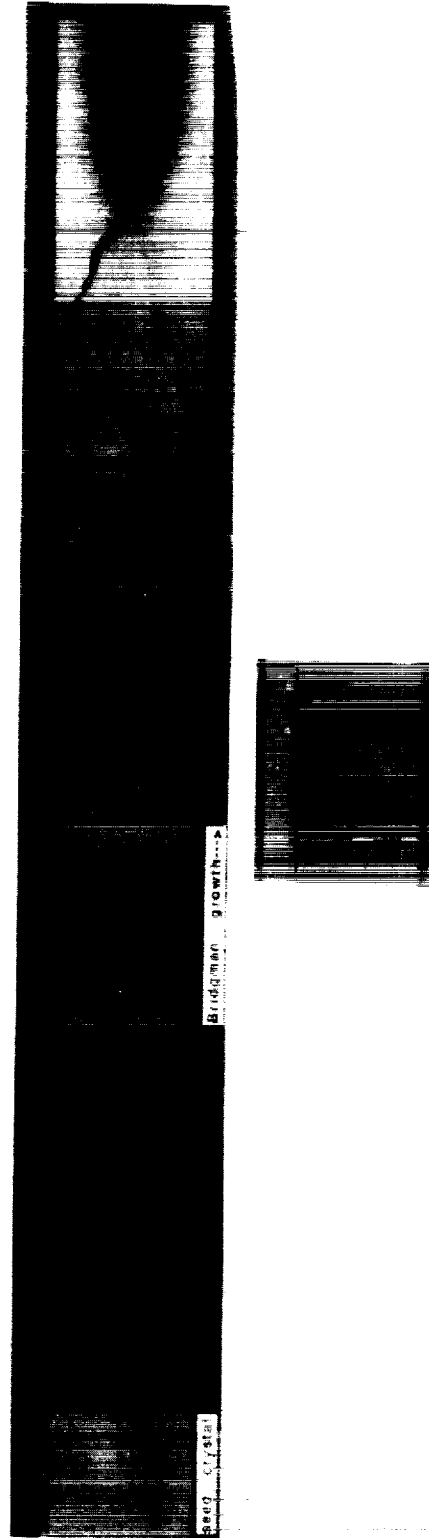


Figure 8 Montage of the infrared transmission imaging for the axial slice from the first ground truth sample.

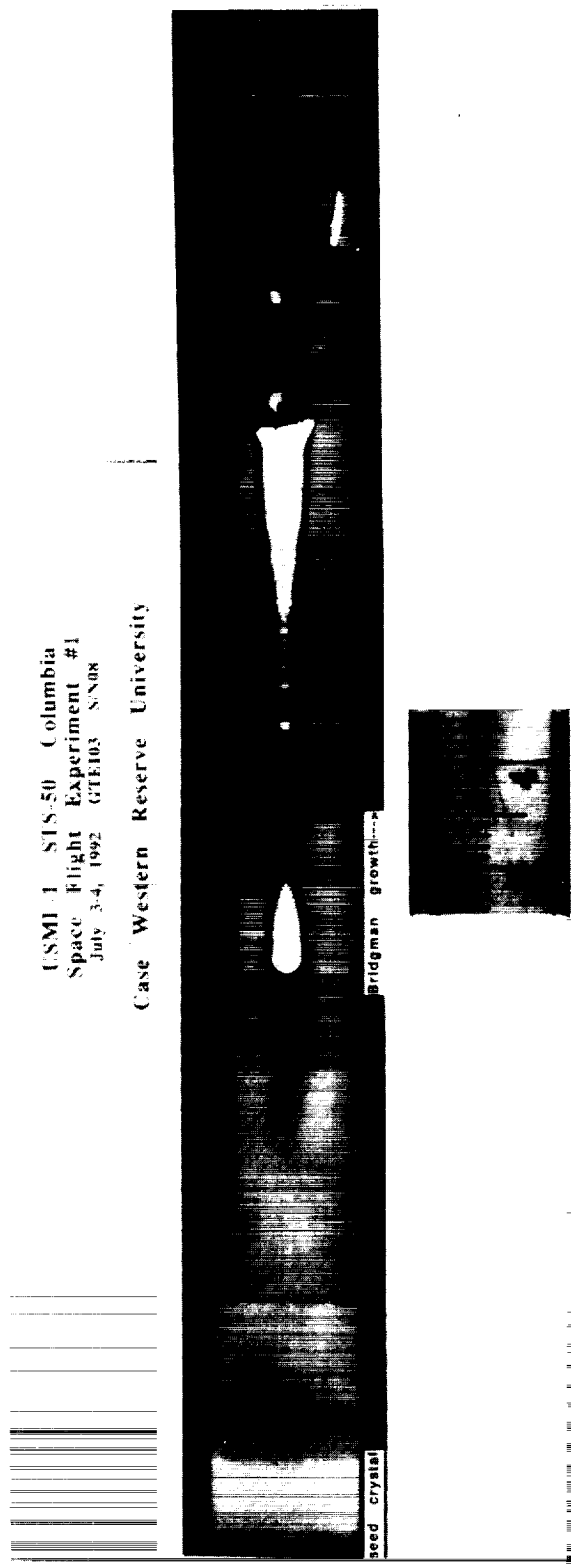


Figure 9 Montage of the infrared transmission imaging for the axial slice from the first flight sample.

USML-1 S/S-50 Columbia
Ground Truth Experiment #2
December 9-10, 1992 GTE-05 3 N10

Case Western Reserve University

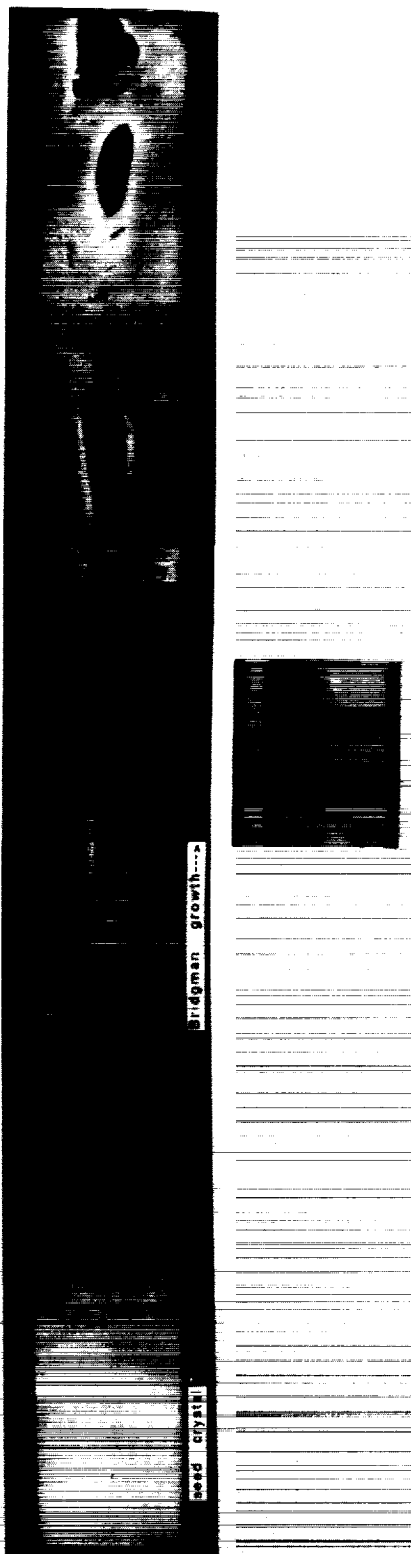


Figure 10 Montage of the infrared transmission imaging for the axial slice from the second ground truth sample.

USML-1 STS-50 Columbia
Space Flight Experiment #2
July 5-6, 1992 GTE106 S102

Case Western Reserve University

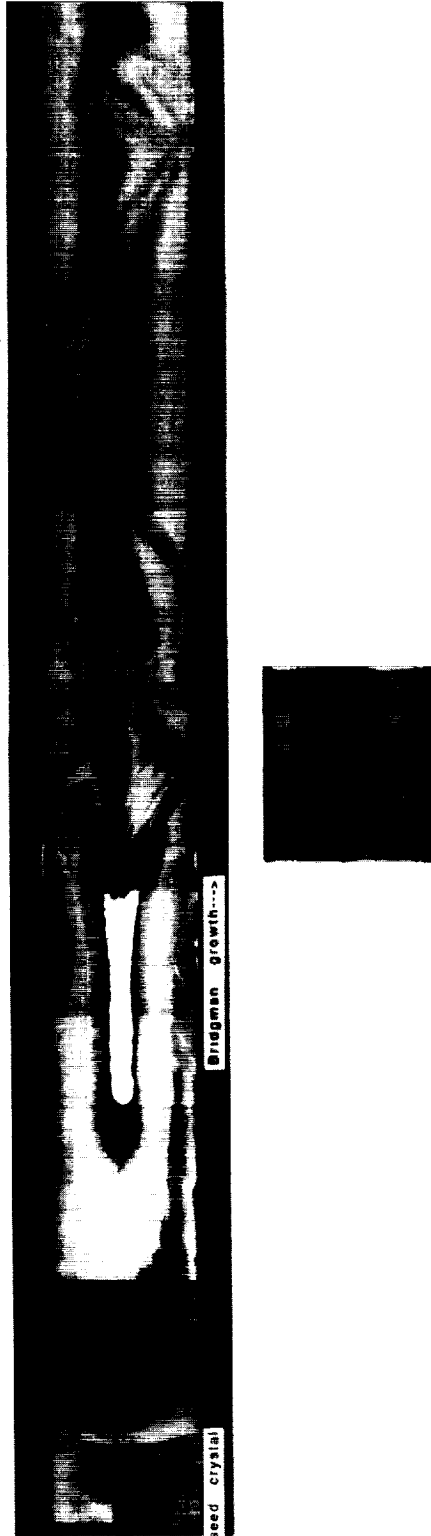


Figure 11 Montage of the infrared transmission imaging for the axial slice from the second flight sample.

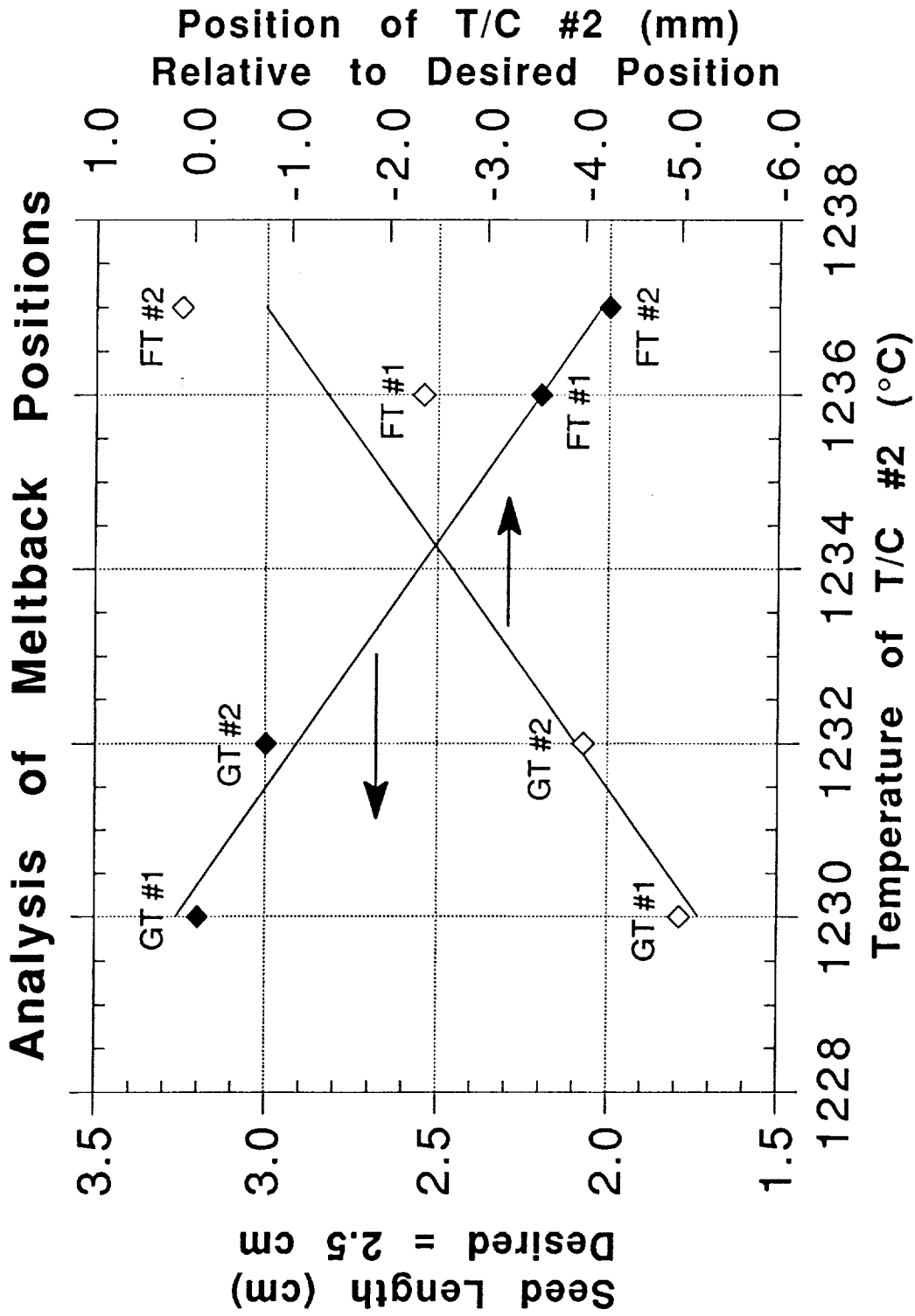


Figure 12 Analysis of the meltback position from the first ground truth (GT#1), first flight (FT#1), second ground truth (GT#2), and second flight (FT#2) samples.

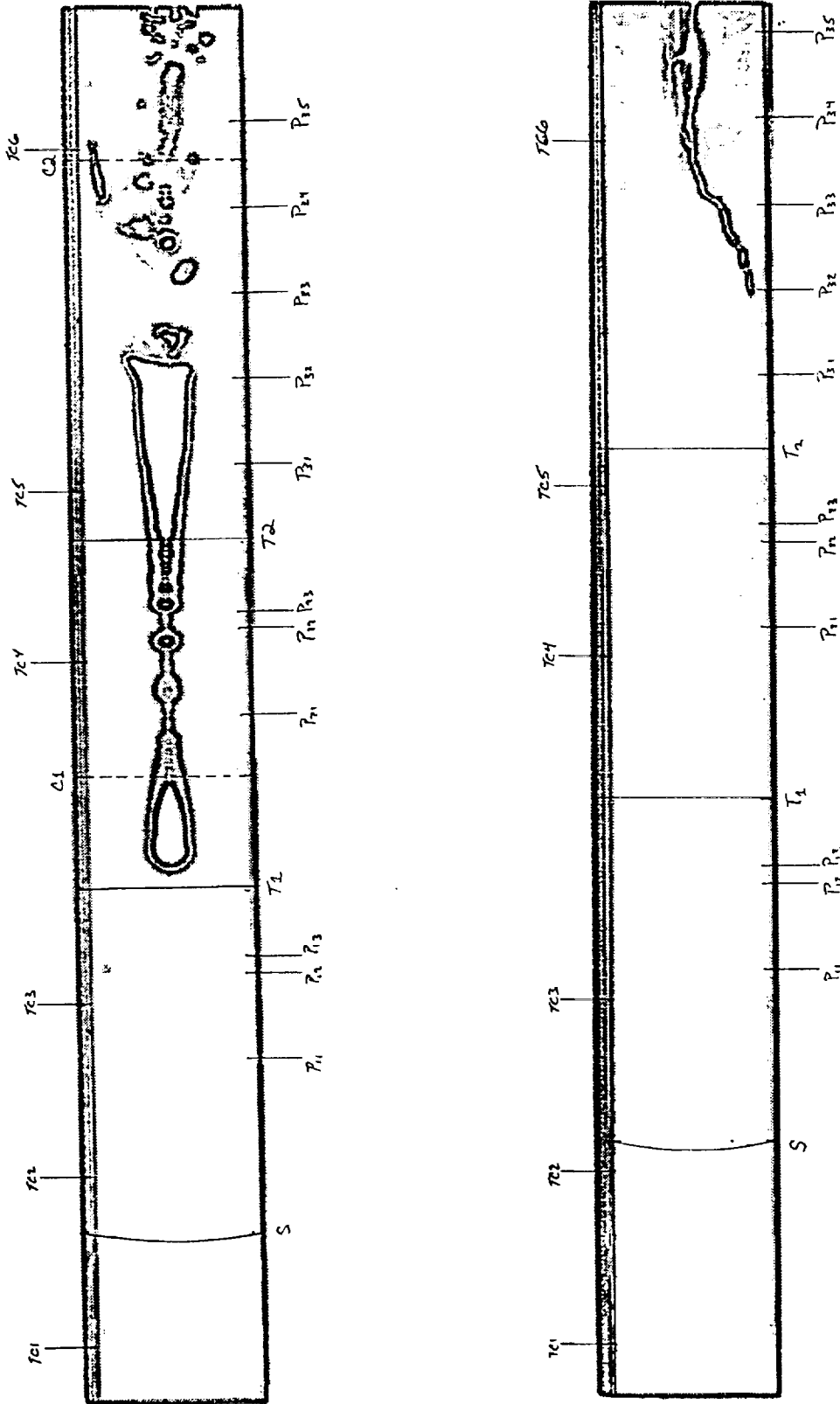


Figure 13 Edge detection image processing of Fig. 8 and Fig. 9. Also shown are the relative positions of the seeding interface (S), initial sample charge positions (Cx), sample thermocouples (TCx), translation rate changes (Tx), and mechanical pulsing events (Pxy).

USML-1 STS-50 Columbia
Ground Truth Experiment #2
December 9-10, 1992 GTF105 S/N10
Case Western Reserve University

USML-1 STS-50 Columbia
Space Flight Experiment #2
July 5-6, 1992 GTF106 S/N02
Case Western Reserve University



Figure 14 Montage of the infra-red microscope imaging of the seeding interface shapes for Fig. 10 and Fig 11.

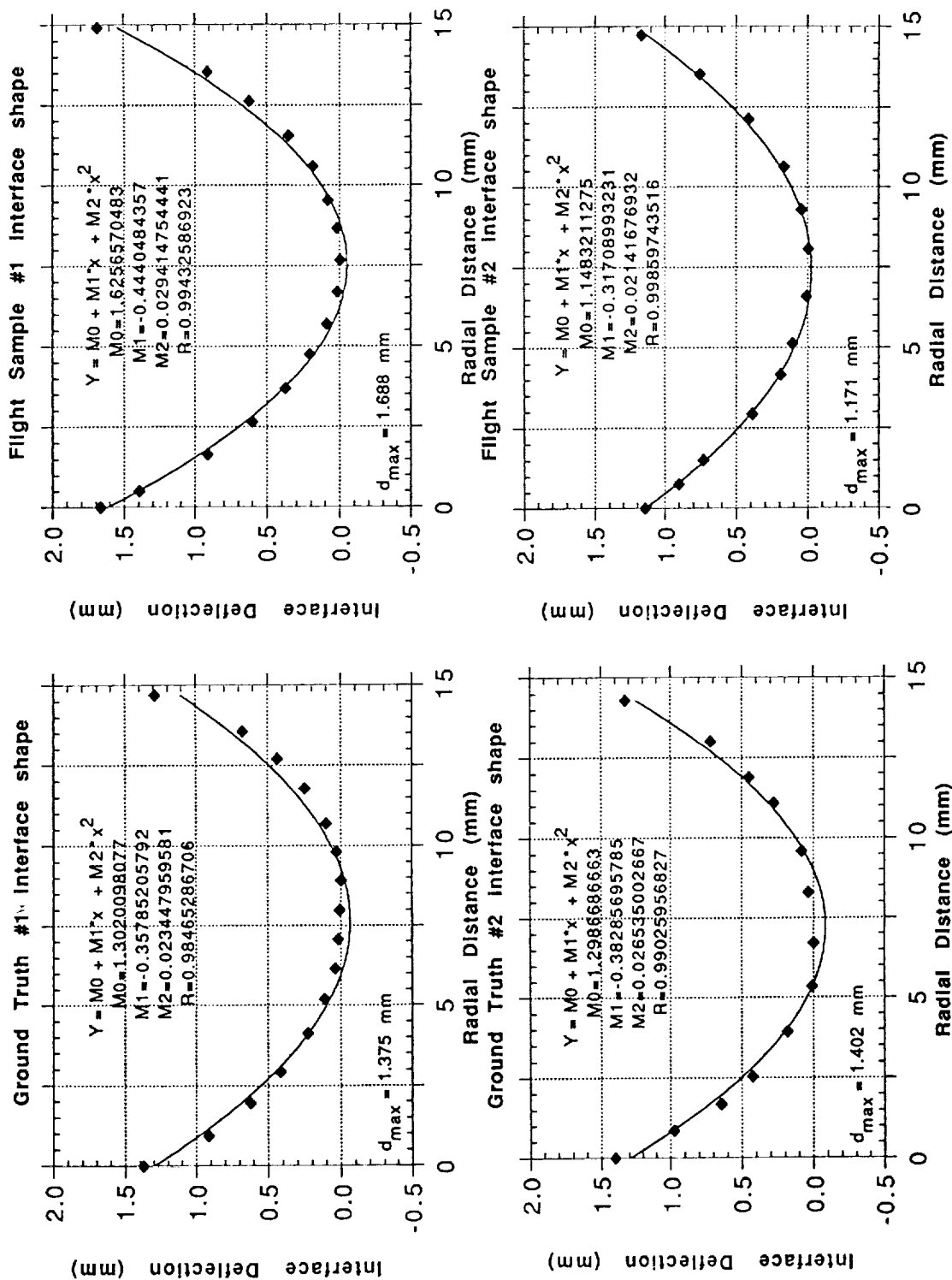


Figure 15 Measured interface shapes for all four samples. Interface shapes are parabolic and symmetric about the growth axis.

Ground Truth Experiment #1
Overall Average Free Carrier Concentration
for 1st Translation

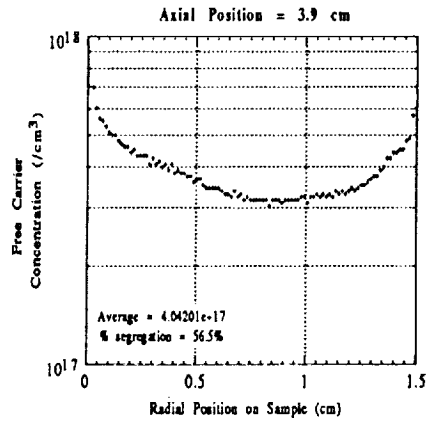
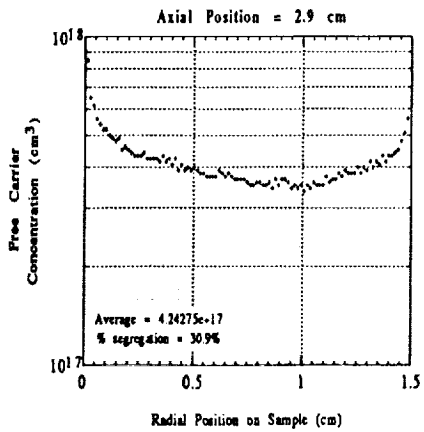
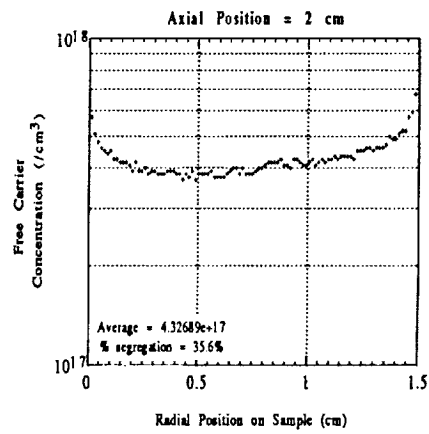
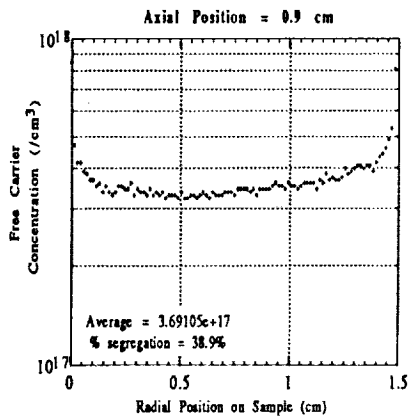
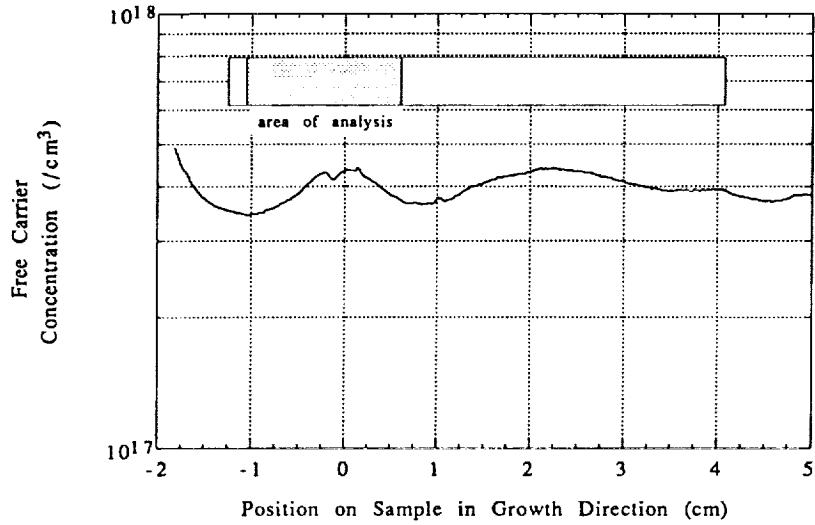


Figure 16 Free carrier concentration (selenium dopant) distribution for the first ground truth sample at the averaged axial positions (top) and for individual radial positions (bottom).

Space Flight Experiment #1
 Overall Average Free Carrier Concentration
 for 1st Translation

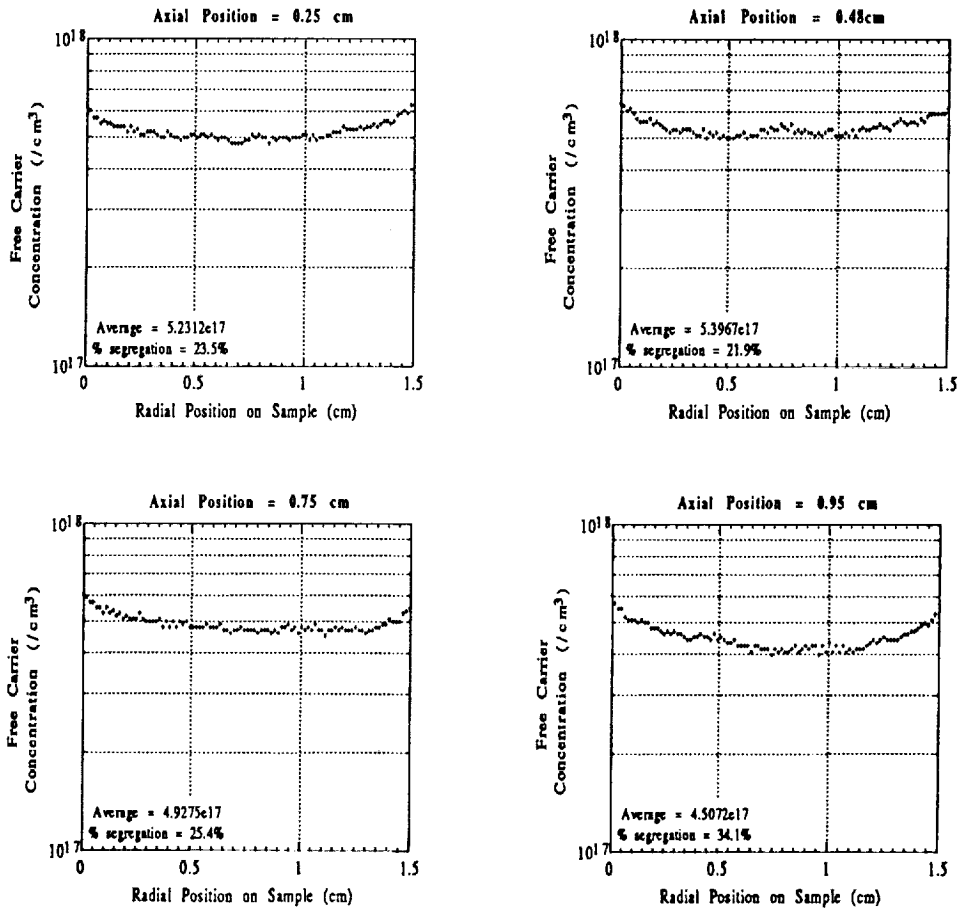
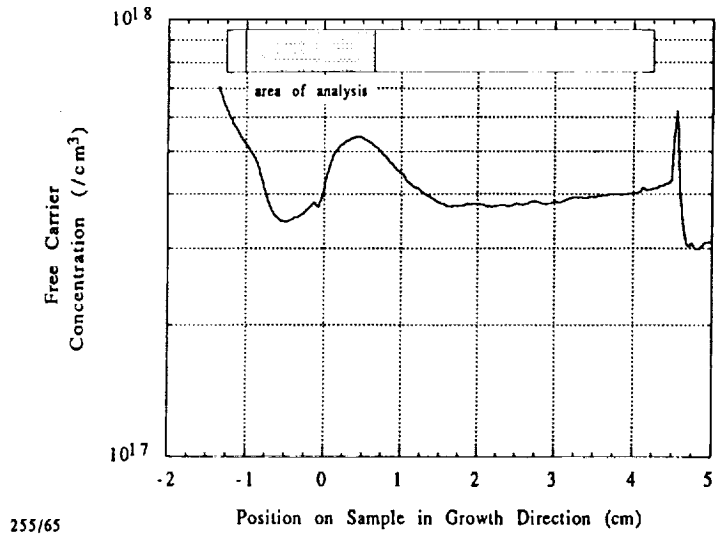


Figure 17a Free carrier concentration (selenium dopant) distribution for the first flight sample at the averaged axial positions (top) and for individual radial positions (bottom).

Space Flight Experiment #1
Overall Average Free Carrier Concentration
for 1st Translation

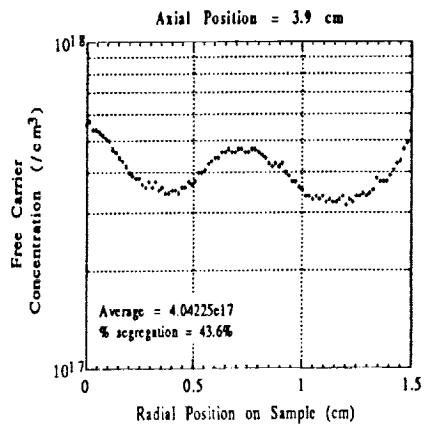
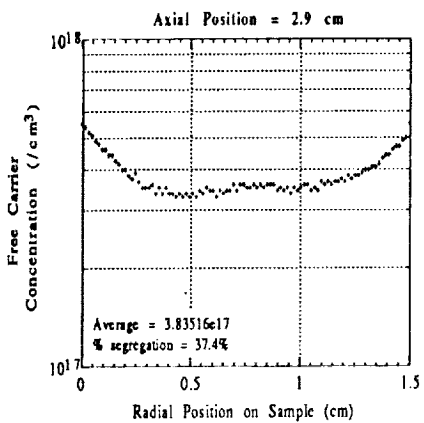
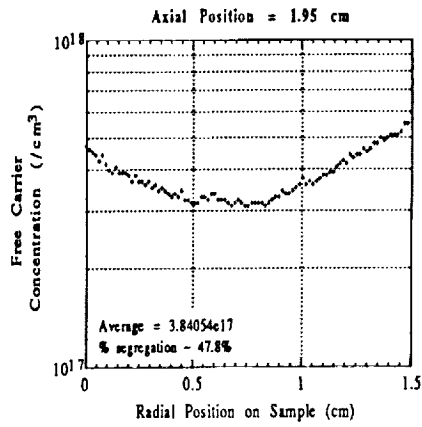
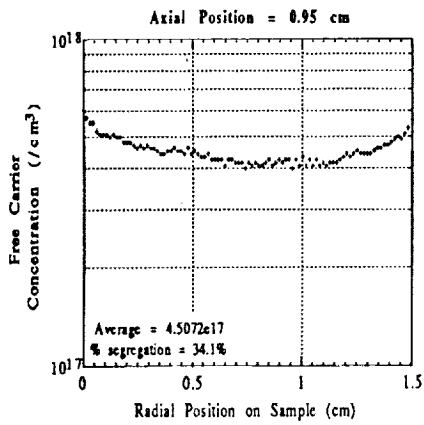
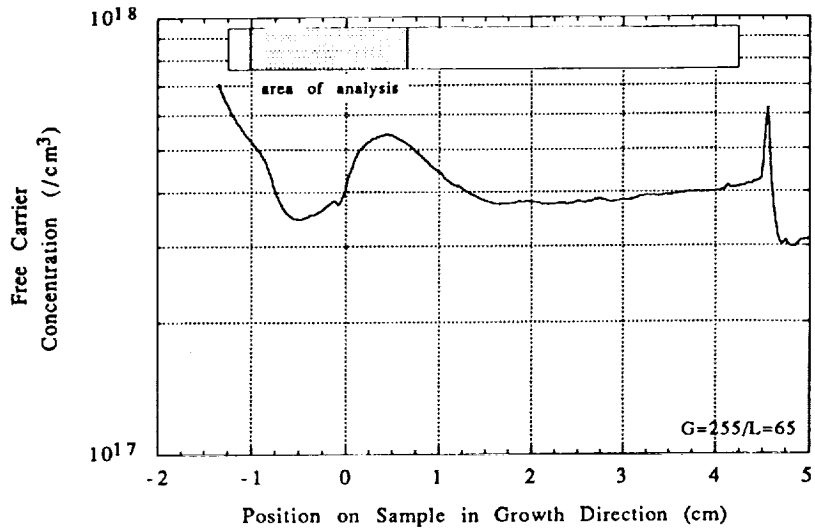


Figure 17b Free carrier concentration (selenium dopant) distribution for the first flight sample at the averaged axial positions (top) and for individual radial positions (bottom).

Ground Truth Experiment #1
Calculated Results from Complete Mixing Equation
Compared to Results from Infrared Imaging

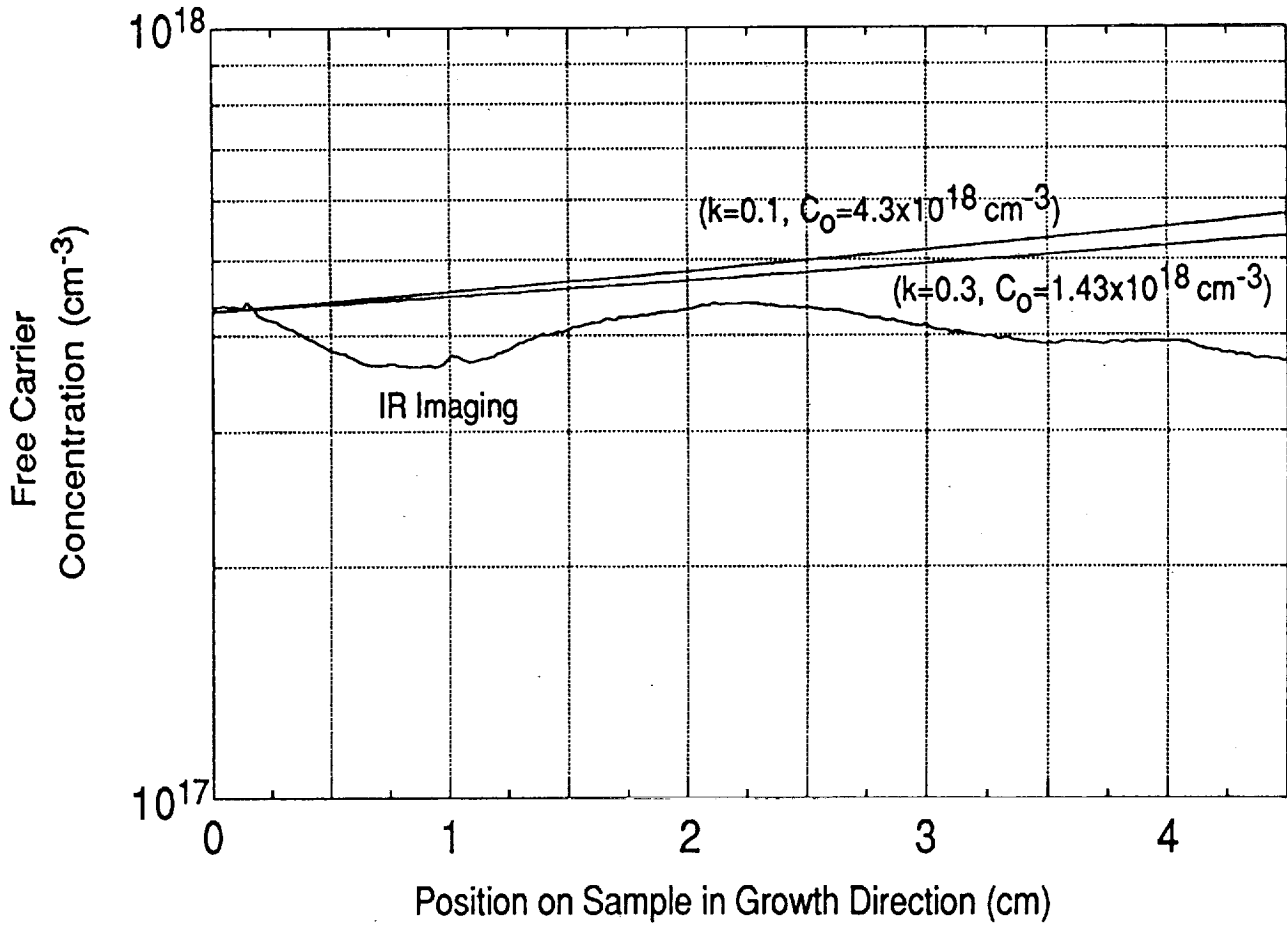


Figure 18 Segregation analysis for the first ground truth sample. Also shown is the segregation behavior for the complete mixing case using the labeled values.

Space Flight Experiment #1
 Theoretical Results from Diffusion-Controlled Growth (DCG)
 and Complete Mixing (CM) Equations Compared with
 Results From Infrared Imaging

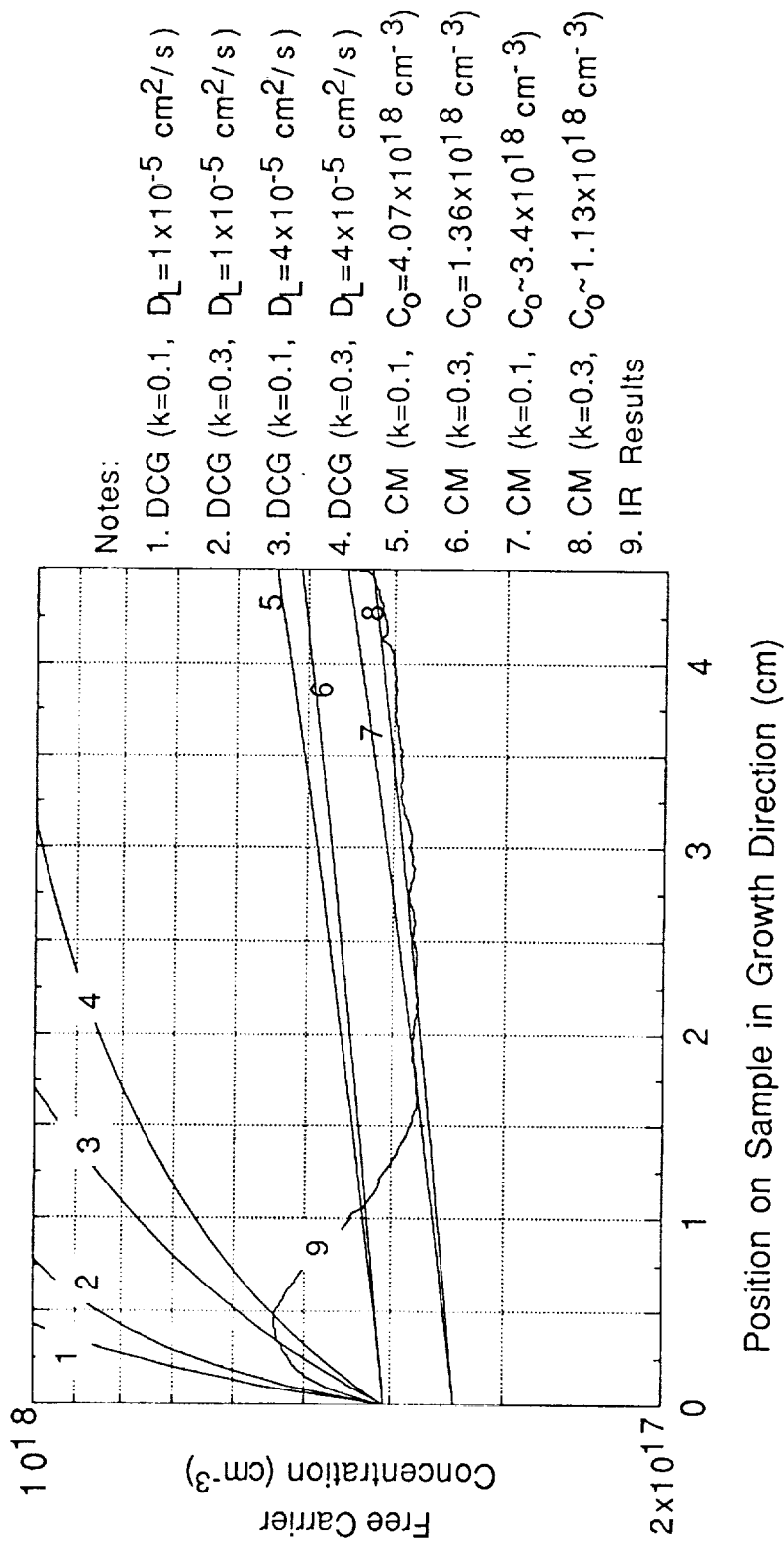


Figure 19 Segregation analysis for the first flight sample. Also shown is the segregation behavior for the complete mixing case and the diffusion controlled growth case using the labeled values.

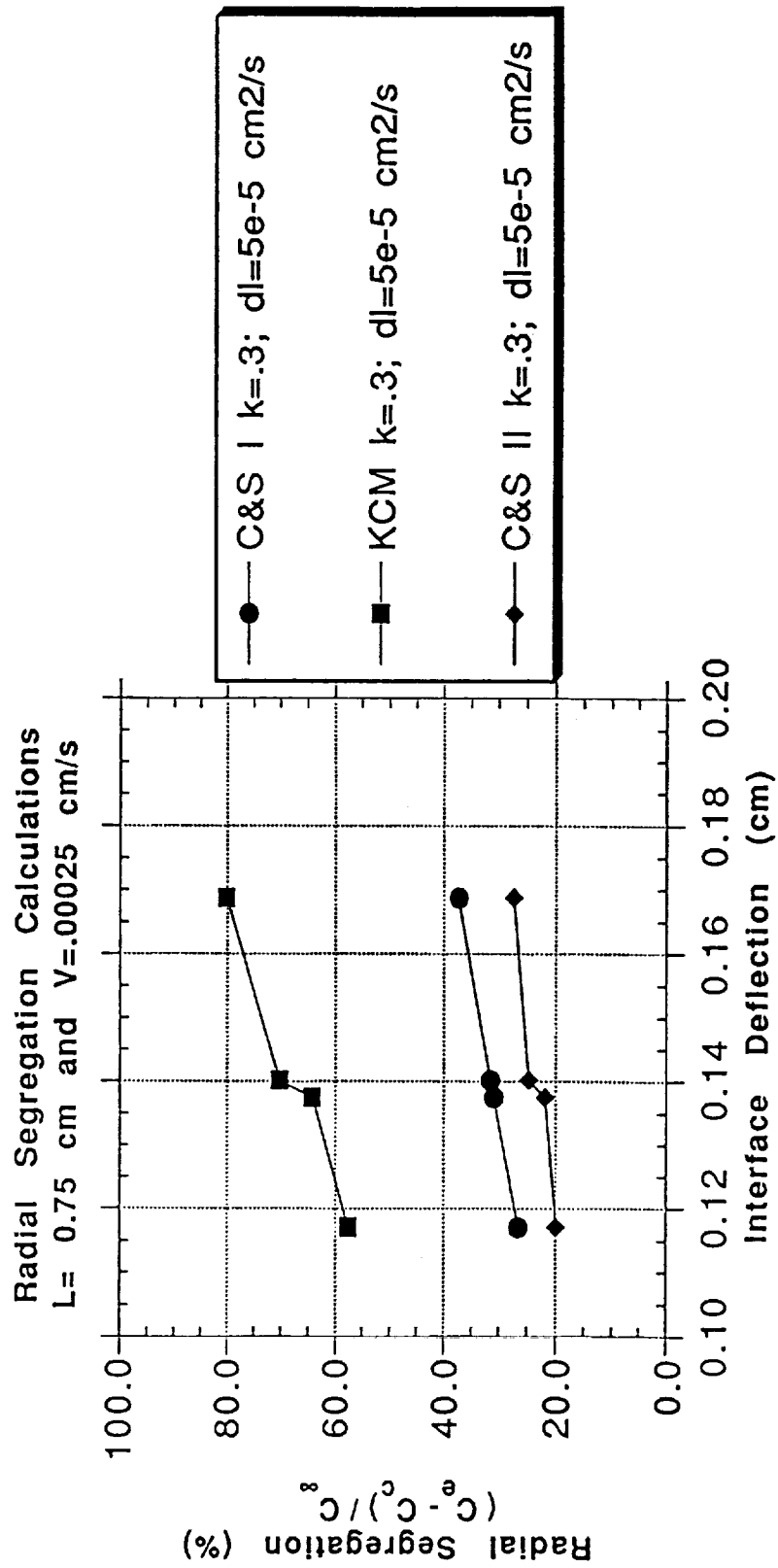


Figure 20 Calculated values for the radial segregation using the various theories (see text).

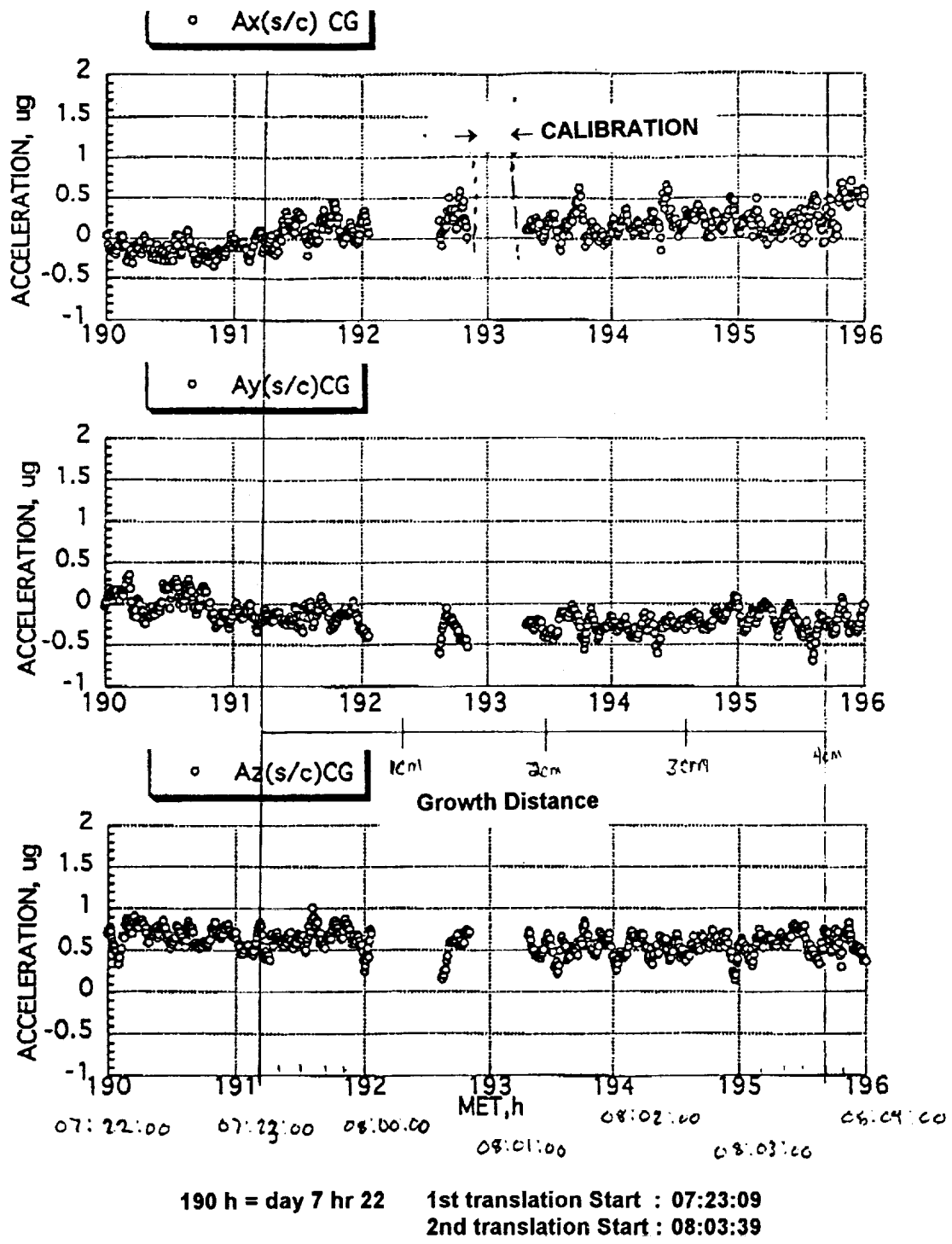
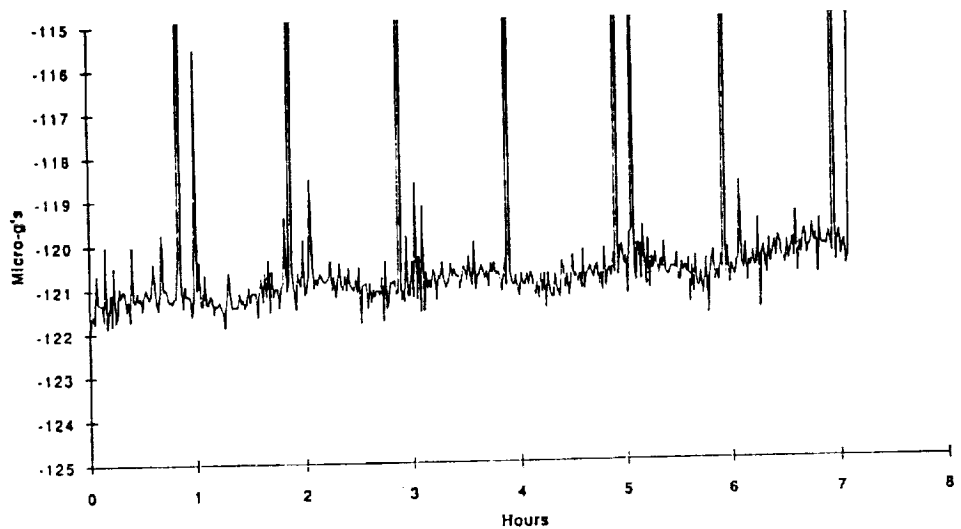
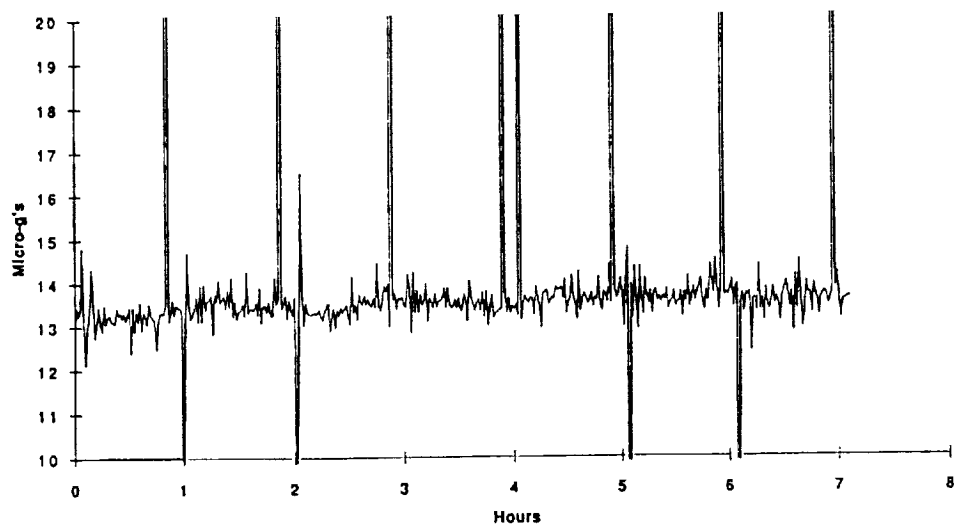


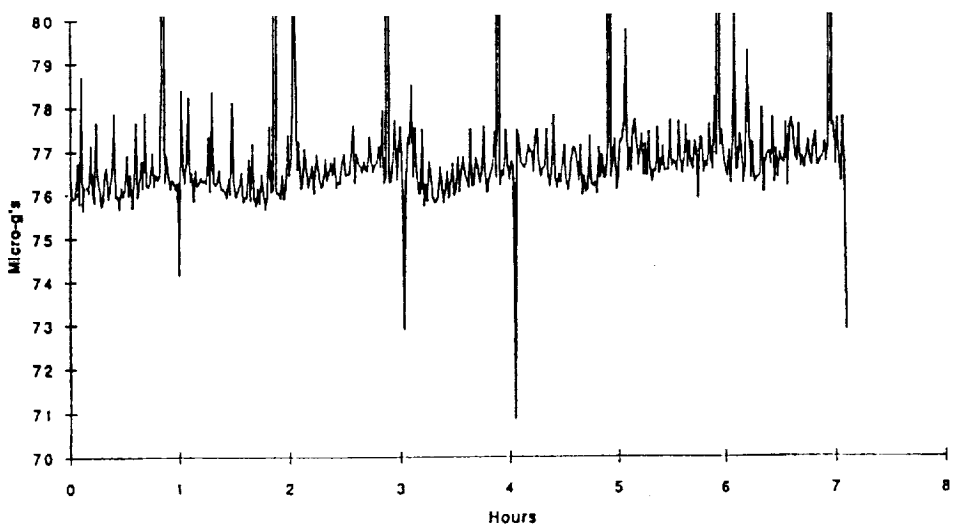
Figure 21 Preliminary acceleration data from the OARE experiment for the first translation period of the first flight sample [22]. Gap in data is due to analysis filtering out of large acceleration deviations.



Detail of X-Axis



Detail of Y-Axis



Detail of Z-Axis

Figure 22 Preliminary acceleration data from the SAMS experiment for the first translation period of the first flight experiment [23]. Note large acceleration peak at the one hour mark.

Discussion

Question: *This smoke plume as you described it, I think, in the second flight sample, can you elaborate or say anything about how that came about ?*

Answer: We are trying to. We have seen it before in a sample when we core the sample. You take a diamond drilling core which is a rather aggressive technique and after we core it, we anneal it, and we have seen in the past that on the slip planes you get precipitates. We are trying to hit one of those with an ogive to find out exactly what it is. Whether it is gallium or whether it is carbon are the two guesses you have and, typically, when we melt back, those don't propagate into the samples. In this case, they did. There was evidence that those precipitates came off on that, indicative of a flow pattern and the dopant distribution measurements also agree that there is a flow pattern. The radial segregation seen is very similar in magnitude to what the ground base was. So to try to alleviate that problem is a problem because we cannot see in the sample externally before we use it. To alleviate that we are working on machining the USML-2 samples with EDM (electro discharge machining).

Question: *Is there any indication of flow in the sample ?*

Answer: I am saying that the plume is indicative of the flow.

Question: *So you do not understand or can't tell us why it (the plume) has that shape ?*

Answer: Right.

Question: *You suggested that an element of a better experiment would be the accurate measurement of the acceleration environment at the experiment. Have you thought, has anybody thought, of going one step beyond that and actually designing an experiment where the acceleration environment is controlled ? Seems like everything is aimed at how good you can do with lesser and lesser micro-g but there seems like there would be value in finding out what small number micro-g's do to you.*

Answer: Well in fact on USML-2, I forget the name of the engineering test demonstration. On USML-2 there will be an attitude change from wings forward to the CGF attitude. It is intended that in that period they will be growing gallium doped germanium crystals with interface demarcation and that crystal will be analyzed to see what does that attitude change do. So yes we have learned that and yes we are going to do that.

Question: *Could you comment on the dopant distribution of those crystals you grow on ground? Do they fit into a diffusion model and things like that ?*

Answer: They follow complete mixing.

Question: *On the ground ?*

Answer: Yes. With interface curvature we have radial segregation around 30-40%.

Question: *This is with regard to your comment about bubble generation. The most common geometry to grow gallium arsenide is the Czochralski geometry which is inverted which you would think would trap bubbles if they were there. Most bubbles that I have read about in cadmium telluride or gallium arsenide seem to show up when there is an abrupt change of rate. What do you think of that possibility ?*

Answer: We have several, we have a theory of the week on bubbles. One theory presented to me was that when you do that growth rate change we are in a rather low gradient situation. You generate such a large heat of fusion that you boil the liquid and you get an arsenic bubble. In generating that arsenic bubble, you change the heat transfer and if you follow the logic, you sort of get to a step growth rate, where it grows rapidly and stops and then grows rapidly and stops. That is a good explanation for why the bubbles are segmented they look like worms actually. They have body segments. And that sort of agrees with the idea, that you had a start and stop growth rate. We are struggling with a way to come up with a definitive experiment to explain it.

Comment: There has been some work done looking at the trapping of inclusions and bubbles and so forth. I think that a theory has been worked out to determine what the critical velocity should be to trap those. I need to go back and refresh myself on that but I sort of thought that looked familiar.

Answer: Yes. In fact we went back to that particular thesis. Yes, we are aware of that and it is a heat transfer problem. When you get the bubble you have to know your heat transfer coefficients which we don't know. Yes, we are aware of that and we are kind of struggling with what numbers do you plug into the theory. .

Question: *Can you say for a certainty whether or not these bubbles are actually voids or whether or not there is some kind of gas inside the bubbles like hydrogen etc. ?*

Answer: I am sure it is a gas and I am sure it is arsenic.

Question: *How are you sure ?*

Answer: Can I prove that statement ? Your comment was am I sure and yes I am sure. Now if you are asking if I can prove that statement the problem you have at temperature is that you have a volatile component in gallium arsenide and that is arsenic. You look at what else we knew we put in there. We put a vacuum on the ampoule and sealed it up. So you have got the graphite, PbN, gallium, arsenic, and you have got the selenium and that's it. You look at what could create that type of bubble.

Question: *That's at room temperature. Is that correct ?*

Answer: Yes, after a low temperature bake out. We do bake it out to make sure we get rid of water vapor. If it was arsenic gas at temperature, it cools down and condenses, it leads back to Don's question, have we gone along to the inside surface to try to find these few micrograms of arsenic that you would expect, and no we haven't and we haven't because we have doubted that we would find it. But we will eventually look. We will see arsenic for sure. Right. But do we see little plates or chunks of arsenic is the question ?